

Chapter 7

Electron Induction Linacs

George J. Caporaso and Yu-Jiuan Chen

Electron induction linacs have been used for over four decades for a variety of applications. As discussed in [Chap. 8](#), these include basic studies in magnetically confined fusion, transport of intense electron beams in various gases, the generation of electromagnetic radiation from free electron lasers, radiation processing of materials and food, and flash X-ray radiography sources.

In this chapter we will discuss the basic structure of electron induction linacs, describe the focusing system commonly used and treat the most important instabilities in these machines.

7.1 Introduction

Typical electron induction linacs incorporate focusing elements into each accelerator cell. Since the induction cells are electrically independent they may be closely placed without affecting their performance. In order to obtain the highest accelerating gradient possible, the usual configuration consists of accelerator cells grouped into blocks of 4–10, which are separated by short sections of transport tube called intercell regions. A typical 4-cell block is shown in [Fig. 7.1](#). Solenoids are typically incorporated into the accelerator cells as can be seen, for example, in [Fig. 6.2](#).

The intercell regions usually provide the pumping ports necessary to ensure adequate vacuum in the accelerator (typical pressures range from 10^{-6} to 10^{-8} Torr in long-pulse machines like DARHT-II). These pumping ports may also provide access for diagnostics such as insertable probes, cameras, etc. Diagnostics such as beam position monitors and current monitors are also generally located in these sections. Solenoids for focusing along with dipole steering coils are also typically found in intercells. The layout of an induction linac (the ETA-II at LLNL) is shown in [Fig. 7.2](#), and the photo of the ETA-II is shown in [Fig. 7.3](#).

G.J. Caporaso (✉)

Lawrence Livermore National Laboratory, Livermore, CA 94550, USA
e-mail: caporaso1@llnl.gov

Fig. 7.1 A 4-cell block is illustrated. The induction cells do not interact electrically and may be placed as closely as possible to achieve maximum accelerating gradient

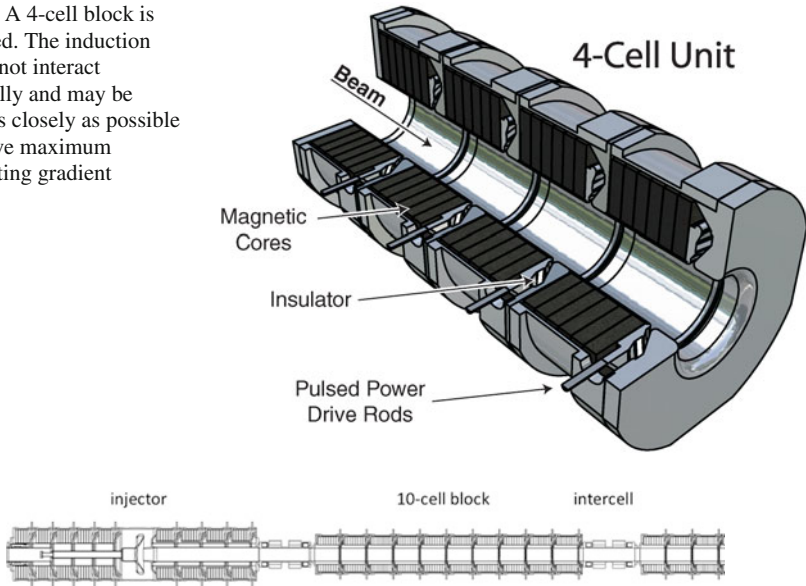


Fig. 7.2 Layouts of the ETA-II accelerator at LLNL is shown above. The machine consists of an injector with 9 induction cells and six 10-cell blocks

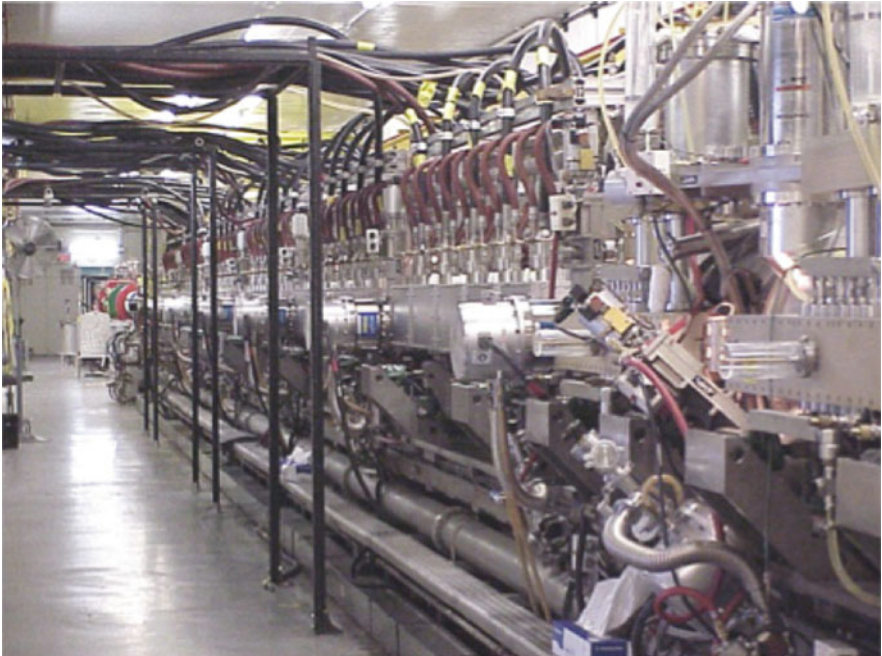


Fig. 7.3 The ETA-II accelerator at LLNL is shown above with the injector in the foreground. This accelerator consists of a 1 MeV injector with 9 induction cells followed by six 10-cell blocks. The machine produces a 5.3 MeV, 2 kA beam with a 50 ns pulsewidth and runs at 1 Hz. It has also operated at 2 kHz in burst mode as discussed in [Chap. 2](#)

The accelerator requires almost continuous focusing along its length to confine the beam against its space charge and to suppress the growth of instabilities. Electron induction linacs use solenoids to focus the beam as they are suitable for cylindrically symmetric beams and are compatible with placement into the induction cells without compromising the accelerating gradient.

The use of focusing is a double-edged sword. Since the focusing elements can never be perfectly aligned and the energy of the beam can never be perfectly constant across the pulse, the beam centroid will develop progressively higher frequency distortions called *corkscrew* as the beam propagates. The beam is also subject to various instabilities as it propagates. Those of most concern are the *image displacement and beam breakup* (BBU) instabilities. Successful strategies to control all of these problems exist and will be described. We will begin by discussing beam formation.

7.2 Electron Sources

7.2.1 Cathodes

Most of the applications of the electron induction accelerators demand high current density beams, which are emitted from a conducting cathode material. There are several approaches that can be used for extracting electrons from the cathode.

Electrons in the cathode material's conduction band need to either surmount or tunnel through the potential barrier, the *work function*, between the conducting material and the vacuum interface before being extracted freely by the electric field in the electron gun. To help these electrons tunnel through the potential barrier, the electric field on the entire emitter surface needs to be in the range of 10^4 kV/cm, which is hard to do. When the electric field on the emitter surface reaches this level, it is very likely that all the conducting electrodes and beam pipe wall in the electron gun are also emitting.

We can provide electrons with additional energy by heating the cathode either with a conventional heat source or an intense laser beam, such that these electrons have large enough kinetic energy to overcome the work function of the material (typically a few tenths of an eV) and escape the surface.

The mechanism for electron emission using a conventional heating method is called *thermionic emission*. The ETA-II injector uses a thermionic dispenser cathode, which is a porous tungsten disk impregnated with $6\text{BaO}-\text{CaO}-2\text{Al}_2\text{O}_3$ and coated with osmium alloy. The coatings on the thermionic cathodes usually lower the work function by roughly 50%. However, they tend to be poisoned easily. The electron gun's vacuum needs to be around 10^{-7} Torr or better. Typically, thermionic dispenser cathodes need to be heated to around $1,100^\circ\text{C}$ in order to provide space charge limited emission, and hence the intrinsic electron temperature is about 0.1 eV. The thermionic emitters have been consistently delivering current density of $10\text{--}100$ A/cm². Their high current density and low intrinsic electron temperature make them a good source for generating high brightness beams. The lifetime for operating at the space charge limited emission region is about 1,000 h at 10 A/cm².

The mechanism for electron emission using a laser is called *photoemission*. So far, this kind of cathode (photocathode) has been used mainly in RF machines, in which the beam pulses are a few picoseconds to a few nanoseconds in length. A space charge limited current at about 90 A/cm^2 over 15 ns was achieved in a feasibility study at LANL [1] with a cathode made of Pb and Al. However, using photoemission to generate longer beam pulses or higher current density beams could be problematic. The high laser intensity (about 1 MW/cm^2) needed to achieve space charge limited emission will create a plasma near the cathode surface and in the anode–cathode gap. The beam quality will then be degraded by this plasma formation. Without degradation by plasma formation, the electron beam’s intrinsic temperature is also about 0.1 eV.

Another approach to generate beams is to reduce the work function of the emitter in situ with electron emission. First, the electric fields are enhanced locally, which leads to field emission (breakdown). The localized breakdown produces a cold, dense plasma arising from adsorbed gasses on the emitter surface. Since plasma has a near zero work function, the anode–cathode gap electric fields can easily extract an electron current from this plasma. This emission mechanism is called *explosive emission*. This type of emitter does not require any additional heating, and is inexpensive. A typical cathode only consists of a piece of ordinary velvet [2] cloth glued with conductive epoxy to a metal plate. Simply apply an electric field greater than 16 kV/cm in the anode–cathode gap. The bound polarization charge at the tip of the dielectric fiber will enhance the electric field at the tip, which leads to plasma formation and subsequent electron emission. Depending on the distribution of the velvet’s tufts, electron emission could be uniform and up to 1 kA/cm^2 . The intrinsic temperature of the emitted electrons is in the range of $0.5\text{--}2 \text{ eV}$ [2, 3]. The plasma gap closure velocity is reasonably low at about $2 \text{ mm}/\mu\text{s}$. Since cathode poisoning is not an issue, the vacuum in the gun region can be 1–2 orders higher than that for thermionic cathodes. Its only obvious disadvantage is that the velvet fibers will erode during a beam pulse. Velvet cathodes have been used in single-pulse machines, such as ATA and on the first axis of DARHT. The lifetime of velvet emitters is about 10^5 shots for regular velvet and 10^6 for velvets coated with a cesium iodide salt [3].

7.2.2 Electron Guns

Figure 7.4 shows the configuration of LLNL’s 1 MeV, 2 kA ETA-II injector. This injector consists of nine induction cells and a diode. There are 5 induction cells to the left of the diode and 4 cells to the right of the diode with the electron beam going to the right. The beampipe and the inner bores of those induction cells at the anode side form a transmission line. Voltage waves created in those cells travel down the transmission line and provide the voltage on the anode electrode. Similarly, the cathode stalk and the inner bores of the induction cells at the cathode side form another transmission line. Voltages generated at those cells would be applied to the cathode. Each induction cell provides a voltage at 111.1 kV, and the total anode–cathode

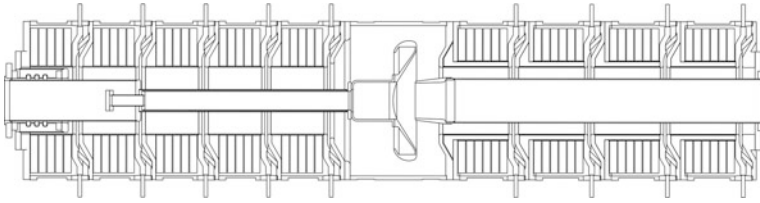


Fig. 7.4 Configuration of LLNL's 1 MeV, 2 kA ETA-II injector

gap voltage is 1 MV. Once the beam enters the anode entrance, the space charge dominated beam will not be accelerated while it propagates in the injector beampipe. One may prefer to minimize the distance that the space charge dominated beam would travel before entering the accelerator by putting all the induction cells at the cathode side. However, the cathode stalk would be long for this configuration, which may be difficult to design and maintain mechanical alignment. To minimize the cathode stalk length by putting all the cells at the anode side is also not desirable since it maximizes the distance that the space charge dominated beam has to travel before being accelerated. The optimal configuration is to minimize the distance between the anode entrance and the accelerator entrance and the cathode stalk length simultaneously. The ETA-II injector, as shown in Fig. 7.4, has 4 cells at the anode side and 5 cells at the cathode.

The ETA-II diode is very similar to the schematic of the diode region shown in Fig. 7.5. The entire system is cylindrically symmetric about the axis of the accelerator. A nonzero canonical angular momentum, an invariant, will lead to an increase of the effective beam emittance. To minimize the canonical angular momentum, one or two bucking coils are used to cancel external focusing magnetic fields at the cathode so that the electrons would be born in a magnetically field-free region. The Pierce-angled cathode shroud is at the same voltage as the cathode and is used

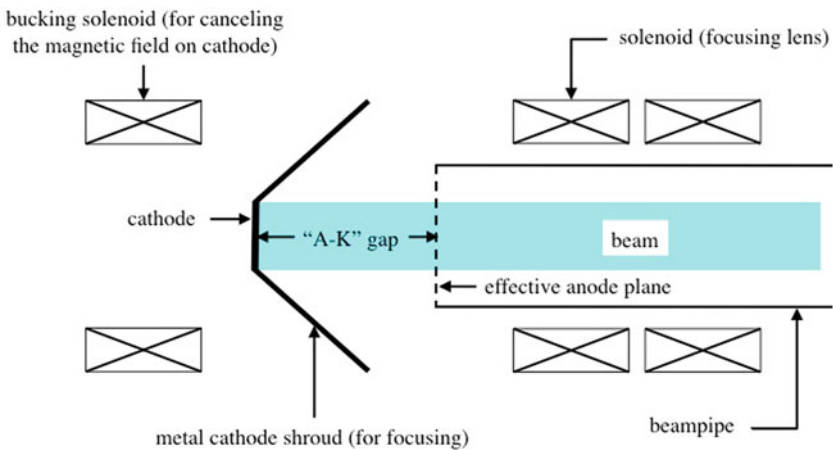


Fig. 7.5 Diagram of a diode region of a typical injector

to shape the potential contours near the cathode. This provides focusing for the electrons in that region and also guides the electrons to, ideally, produce a laminar flow. Once the extracted beam leaves the area immediate to the cathode surface, it is held together (focused) by an array of solenoids wrapped around the anode pipe. Although the detailed geometry of the diode configuration will affect the emitted current density, the Child-Langmuir law for space charge limited current density emitted from a planar diode given as

$$J_0 = \frac{4}{9} \sqrt{\frac{2e}{m}} \frac{\epsilon_0 V_0^{3/2}}{d^2} = \frac{2.33 \times 10^{-6} V_0^{3/2}}{d^2} \quad (7.1)$$

provides a reasonable estimation for the emitted current density [4, 5]. Note that the Child-Langmuir law describes the emission of a non-relativistic beam. H. Ivey provided a modified space-charge-limited emission law for a relativistic beam [6]. As shown in Fig. 7.6, the relativistic effects suppress the electron emission somewhat.

Generally, to obtain a small emittance and high current beam, the cathode area should be small while the field stress in the diode region should be high. This may lead to unwanted emission from electrodes due to excessive field stress on the electrode surfaces. While electrons emitted at the tip of the shroud, where the field stress is largest, cannot enter the anode entrance and spoil the beam emittance, electrons emitted from the shroud near the cathode can easily be captured and phase-mixed with the beam. These electrons are born at a large angle, θ_{sh} with respect to the laminar flow. They can greatly increase the beam emittance. Figure 7.7 shows PIC simulations of how a small fraction of electrons, 0.8% of the total ETA-II beam current, emitted from the inner radius of the shroud are captured by the beam as it is transported between the cathode and anode [7]. These unwanted electrons cause large emittance growth. Let n be the fraction of beam current field-emitted from the shroud with respect to the total extracted current. The factor of emittance growth is approximately given by $1 + n\theta_{sh}/\theta_{th}$, where θ_{th} is the intrinsic thermal angle of electrons emitted from the cathode. To avoid this source of emittance growth, injectors should use larger area cathodes with minimum field stress. Also, the shroud electrode should be made of a material that is resistant to electron emission.

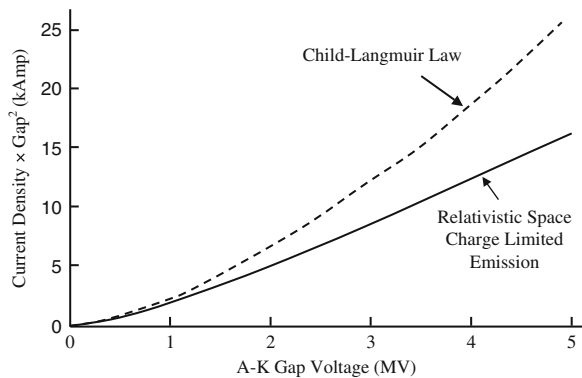


Fig. 7.6 Comparison of the relativistic space-charge-limited current and Child-Langmuir law

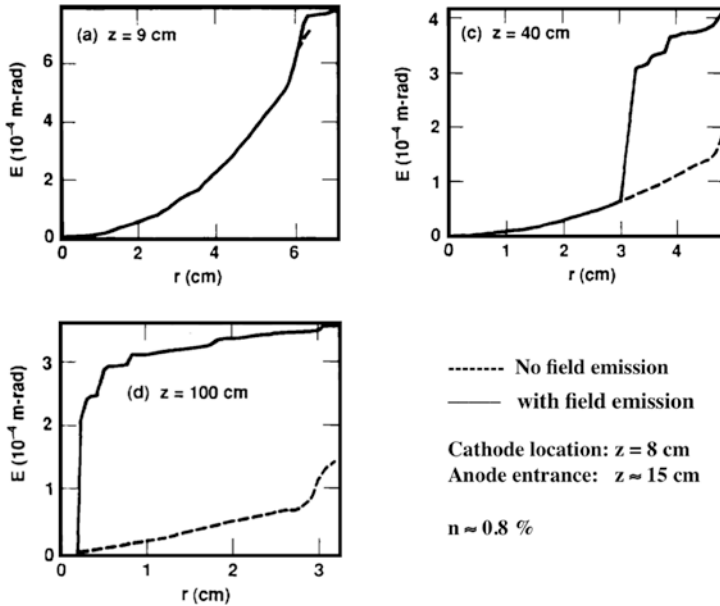


Fig. 7.7 Normalized emittance, E , of the enclosed beam within radius r vs. r is plotted with and without the presence of field emitted electrons from the shroud. The plots, given at various transport distances, show the degradation of beam emittance resulting from mixing in a small number of field-emitted electrons from the shroud (0.8% of the total beam)

7.3 Beam Dynamics in Induction Machines

7.3.1 Basic Force Equation

We wish to consider the motions of both individual charged particles and collections of charged particles (beams). The motions of all particles, charged or otherwise, are governed by

$$\frac{d\mathbf{p}}{dt} = \mathbf{F}, \tag{7.2}$$

where \mathbf{F} is the force vector which acts on the particle whose momentum vector is given by \mathbf{p} . This equation holds for all forces and is valid for relativistic as well as non-relativistic motion (note that the familiar $m\mathbf{a} = \mathbf{F}$ is just a special case of Eq. (7.2), which is valid when the mass is constant). For a charged particle with charge q the force is just given by the *Lorentz Force*

$$\mathbf{F}_L = q[\mathbf{E} + \mathbf{v} \times \mathbf{B}], \tag{7.3}$$

where \mathbf{E} is the electric field and \mathbf{B} is the magnetic field.

For an electron moving along the z -axis and subject to only transverse forces the equation of motion becomes

$$\gamma_b m_e \frac{d\mathbf{v}}{dt} = -e[\mathbf{E} + \mathbf{v} \times \mathbf{B}]_{\perp}, \quad (7.4)$$

where the subscript on the Lorentz force indicates that we are just taking the transverse component. Here

$$\gamma_b = \frac{1}{\sqrt{1 - \frac{v^2}{c^2}}} \quad (7.5)$$

and $\gamma_b m_e$ is the “transverse mass”. If acceleration is present (due to a z -component of electric field from an accelerating cell for instance), then we must replace the left hand side of Eq. (7.4) by $d(\gamma_b m_e \mathbf{v})/dt$. From this point on, we will assume that we have purely transverse forces.

A very important case in practice, is that of transverse velocities being small compared to the longitudinal velocity. Equivalently, whenever $\partial x/\partial z$ and $\partial y/\partial z$ are *both* substantially less than 1, we speak of the motion as being “paraxial” (nearly parallel to the axis). This is frequently the case for a relativistic particle and allows us to simplify the dynamics by replacing t with z as the independent variable in the force equation.

If $v_{\perp}^2/v^2 \ll 1$, then we have that $v_z \simeq v$ (in practice this is usually a good approximation if $\partial x/\partial z \leq 1/3$). Under these conditions, we can write

$$\frac{d}{dt} \simeq v \frac{d}{dz} \simeq v_z \frac{d}{dz} \quad (7.6)$$

for a single particle.

With this approximation, we may rewrite the equation of motion (7.4) as

$$\gamma_b \beta^2 m_e c^2 \frac{d^2 \mathbf{r}}{dz^2} = -e[\mathbf{E} + \mathbf{v} \times \mathbf{B}]_{\perp}, \quad (7.7)$$

where \mathbf{r} is the transverse position vector.

7.3.2 Coordinate Description of a Beam

We wish to consider the analog of Eq. (7.7) that is appropriate for a collection of particles (a beam) instead of just one. If we had N particles in our beam, we could just hang a subscript on \mathbf{r} and write Eq. (7.7) for each of them.

We could also regard the beam as a continuous fluid. In this case, the beam dynamics will be a function of time (or equivalently, z) and some other quantity

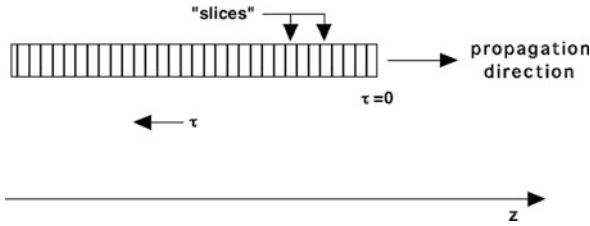


Fig. 7.8 Beam coordinate system

that labels the position of the particle along the beam. We will imagine that the beam can be divided into imaginary “slices” labeled by a coordinate τ that has the definition (see Fig. 7.8)

$$\tau \equiv t - \frac{z}{v}. \quad (7.8)$$

τ is usually defined so that it is zero at the front or head of the beam and increases toward the tail.

The quantity τ is a local coordinate in the beam frame (i.e., if you were riding along with the beam, τ would measure the distance back from the head of the beam divided by v). Another way to think of τ is that if you had an array of beam position monitors along the accelerator that you were examining with oscilloscopes, the time axis on each scope trace would actually be τ . In general, all quantities we would want to compute are functions of z and τ . So if we have some function $f(z, \tau)$, then its total time derivative is

$$\frac{df(z, \tau = t - z/v)}{dt} = \left. \frac{\partial f}{\partial z} \right|_{\tau} \frac{dz}{dt} + \left. \frac{\partial f}{\partial \tau} \right|_z \left(\frac{dt}{dt} - \frac{1}{v} \frac{dz}{dt} \right) = v \left. \frac{\partial f}{\partial z} \right|_{\tau}, \quad (7.9)$$

and our analog of Eq. (7.7) for a continuous beam becomes simply

$$\gamma_b \beta^2 m_e c^2 \frac{\partial^2 \mathbf{r}(z, \tau)}{\partial z^2} = -e[\mathbf{E} + \mathbf{v} \times \mathbf{B}]_{\perp}. \quad (7.10)$$

7.3.3 Focusing in a Solenoidal Field

Let us consider a solenoid [8] that is one of the most commonly used focusing systems for electrons (virtually all electron induction accelerators use solenoidal focusing).

Because the magnetic field lines must close on themselves (since the divergence of \mathbf{B} is zero), there must be a radial as well as an axial component of field in a finite length solenoid:

$$\mathbf{B} = \hat{\mathbf{e}}_r B_r + \hat{\mathbf{e}}_z B_z. \quad (7.11)$$

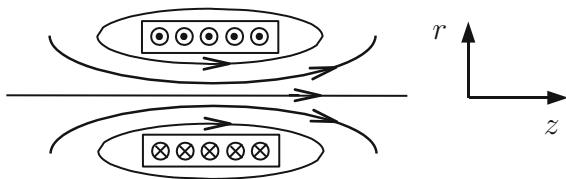


Fig. 7.9 Schematic of a solenoid with current coming out of the page in the upper plane and entering the page in the lower plane. The *curves* wrapping around the solenoid indicate the magnetic field lines

We can estimate this radial field by using the fact that the divergence of the magnetic field vanishes. We have (with no azimuthal field)

$$\nabla \cdot \mathbf{B} = 0 = \frac{1}{r} \frac{\partial}{\partial r} (r B_r) + \frac{\partial B_z}{\partial z}. \quad (7.12)$$

Now near the z -axis, we have approximately that

$$B_r \simeq -\frac{r}{2} \frac{\partial B_z(z, 0)}{\partial z}, \quad (7.13)$$

where we have integrated Eq. (7.12) with respect to r by taking the z -derivative of B_z to be a constant (at its on-axis value). The radial component causes a divergence of the field lines at either end of the solenoid. These are referred to as “fringe fields” and are illustrated in Fig. 7.9. The normalized B_z field and B_r/r are plotted in Fig. 7.10.

Solenoids can focus a beam and confine the transverse motion of its centroid. We will consider the idealized case of a continuous, constant solenoidal field (in actuality, the focusing is provided by many discrete solenoids usually placed so close together that the field is treated as continuous to a first approximation). The case of a magnetic field that varies in z can be treated by the same methods but is somewhat more complicated. In what follows, we will consider only a constant field. In that case, the magnetic field is just

$$\mathbf{B} = \hat{e}_z B_0. \quad (7.14)$$

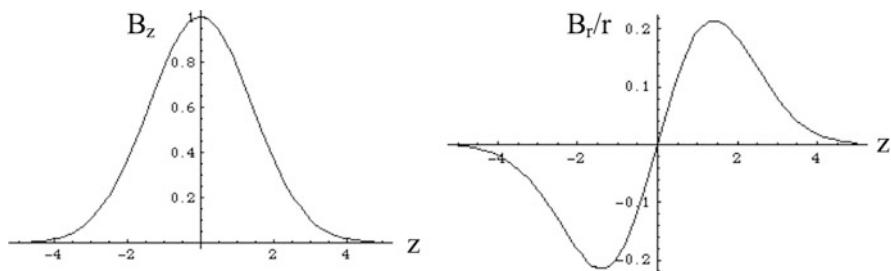


Fig. 7.10 Plots of the normalized z and r components of the field of a solenoid

The equation of motion just becomes

$$\gamma_b \beta^2 m_e c^2 \frac{\partial^2 \mathbf{r}}{\partial z^2} = -e \mathbf{v} \times \mathbf{B}. \quad (7.15)$$

Using Eq. (7.14), this becomes

$$\frac{\partial^2 \mathbf{r}}{\partial z^2} = -\frac{e}{\gamma_b \beta^2 m_e c^2} \left[\beta c \frac{\partial x}{\partial z} \hat{\mathbf{e}}_x + \beta c \frac{\partial y}{\partial z} \hat{\mathbf{e}}_y + \beta c \hat{\mathbf{e}}_z \right] \times \hat{\mathbf{e}}_z B_0. \quad (7.16)$$

Retaining only transverse components of force, this becomes

$$\frac{\partial^2 \mathbf{r}}{\partial z^2} = -\frac{e B_0}{\gamma_b \beta m_e c} \left[-\hat{\mathbf{e}}_y \frac{\partial x}{\partial z} + \hat{\mathbf{e}}_x \frac{\partial y}{\partial z} \right]. \quad (7.17)$$

Finally, these can be simplified as

$$x'' + k_c y' = 0, \quad (7.18)$$

and

$$y'' - k_c x' = 0, \quad (7.19)$$

where a prime denotes differentiation with respect to z and where we define the *cyclotron wavenumber* k_c as

$$k_c \equiv \frac{e B_0}{\gamma_b \beta m_e c} = \frac{B_0(\text{kg})}{1.703 \gamma_b \beta} (\text{cm}^{-1}). \quad (7.20)$$

The cyclotron wavenumber is a measure of the focusing strength of the solenoid.

The easiest way to solve the coupled set of Eqs. (7.18) and (7.19) is to use *phasors*. A phasor is a complex quantity that we can use to combine Eqs. (7.18) and (7.19) into a single equation. We define the phasor ξ as

$$\xi \equiv x + iy. \quad (7.21)$$

Multiplying Eq. (7.19) by i and adding it to Eq. (7.18) and using the definition (7.21), we have

$$\xi'' - i k_c \xi' = 0. \quad (7.22)$$

Once we solve Eq. (7.22), we can immediately find x and y as

$$x = \text{Re}(\xi), \quad (7.23)$$

and

$$y = \text{Im}(\xi), \quad (7.24)$$

The solution to Eq. (7.22) is just

$$\xi = A + B e^{ik_c z}, \quad (7.25)$$

where A and B are complex constants that will be determined by the initial conditions on x , y , x' and y' . We have

$$\xi(0) = x(0) + iy(0) = A + B, \quad (7.26)$$

while

$$\xi'(0) = x'(0) + iy'(0) = ik_c B. \quad (7.27)$$

Thus

$$\xi(z) = \xi(0) + \frac{i\xi'(0)}{k_c} - \frac{i\xi'(0)}{k_c} e^{ik_c z}. \quad (7.28)$$

Taking the real and imaginary parts and using Eqs. (7.26) and (7.27), we find that

$$x(z) = x(0) - \frac{y'(0)}{k_c} + \frac{y'(0)}{k_c} \cos k_c z + \frac{x'(0)}{k_c} \sin k_c z, \quad (7.29)$$

and

$$y(z) = y(0) + \frac{x'(0)}{k_c} - \frac{x'(0)}{k_c} \cos k_c z + \frac{y'(0)}{k_c} \sin k_c z. \quad (7.30)$$

Let us consider a simple example with $x(0) = y(0) = x'(0) = 0$ and $y'(0) = y'_0$. Then we have

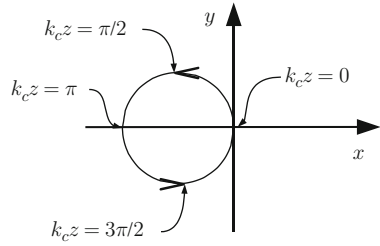
$$x(z) = -\frac{y'_0 [1 - \cos k_c z]}{k_c}, \quad (7.31)$$

and

$$y(z) = \frac{y'_0}{k_c} \sin k_c z. \quad (7.32)$$

Projected onto the x - y plane, this motion is just a circle. In the laboratory frame the orbit describes a helix since it is advancing in z .

Fig. 7.11 Projection of the particle orbit onto the x - y plane for the example in the text



It is not clear how the motion depicted in Fig. 7.11 describes focusing. We will find that when viewed from a special reference frame this motion will appear intuitively to provide focusing. We will first do this mathematically and then show how it works physically.

Let us return to Eq. (7.22) and solve it in another way. We can remove the first derivative by use of a standard mathematical trick. We define a new dependent variable Ω such that

$$\xi = \Omega e^{\frac{ik_c z}{2}}, \tag{7.33}$$

and substitute it into Eq. (7.34). We have

$$\xi' = \left(\Omega' + \frac{ik_c \Omega}{2} \right) e^{\frac{ik_c z}{2}}, \tag{7.34}$$

and

$$\xi'' = \left(\Omega'' + ik_c \Omega' - \frac{k_c^2 \Omega}{4} \right) e^{\frac{ik_c z}{2}}. \tag{7.35}$$

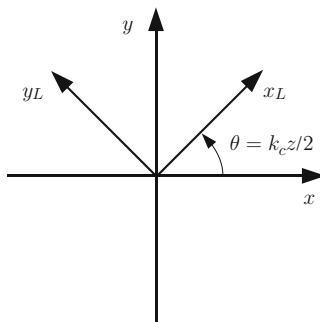
Substitution of these expressions into Eq. (7.22) yields

$$\Omega'' + \frac{k_c^2 \Omega}{4} = 0. \tag{7.36}$$

We note that Eq. (7.36) is a harmonic oscillator equation with *betatron wavenumber* given by $k_c/2$. What we have done with the transformation given by Eq. (7.33) is to go into a rotating reference frame that is spinning with angular “velocity” given by $k_c/2$ which is called the *Larmor wavenumber* or “frequency” (the rotating frame is called the Larmor frame). When viewed in this frame, the motion described by Eqs. (7.31) and (7.32) is an oscillatory motion in a single plane, which goes through the origin. Figure 7.12 shows the Larmor frame and its relationship to the laboratory frame.

Let us reexamine the motion shown in Fig. 7.11. We will label various points corresponding to increments of $k_c z$ equal to $\pi/2$ in both the laboratory and Larmor frames as shown in Fig. 7.13.

Fig. 7.12 The Larmor frame and its relationship to the laboratory reference frame



The orbit starts at position 1 which is at the origin in both coordinate systems. By the time the particle has advanced to position 2 in the lab frame, the Larmor frame has rotated by such an amount that the particle is along its positive y-axis. By position 3, the Larmor frame has rotated counter-clockwise by 90° so that position 3 appears further out along its positive y-axis. By position 4, the electron appears to be moving down along the positive y-axis of the Larmor frame, and by the time the electron has moved to position 5, it has completed one cyclotron orbit in the lab frame *but only half a betatron orbit in the Larmor frame*. At this point the Larmor frame has rotated 180° counter-clockwise so that the negative-y axis is pointing “up” in the lab frame. Therefore, as the electron makes its second orbit in the lab frame, it will be seen to move up and down along the negative y-axis in the Larmor frame. Upon completion of its second orbit, the Larmor frame would have rotated a full 360°. This picture is essentially unchanged even if the magnetic field changes with propagation distance.

Thus far we have looked at the focusing effect of an electron in a constant, axial field, and we found that transverse components of velocity were needed in order for there to be any transverse force components. If the electron is moving purely parallel to the field, no forces will be generated. Of course, real focusing systems have solenoids of finite length so that there will be fringe fields. These fringe fields will give rise to transverse components of velocity, which the main, axial field can

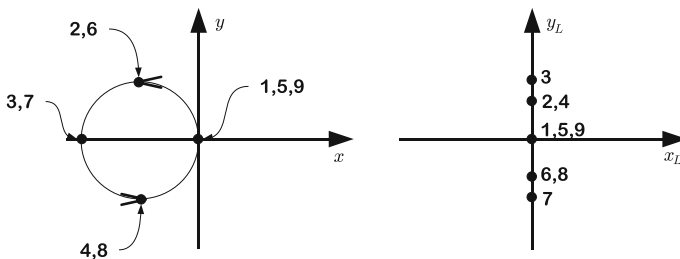
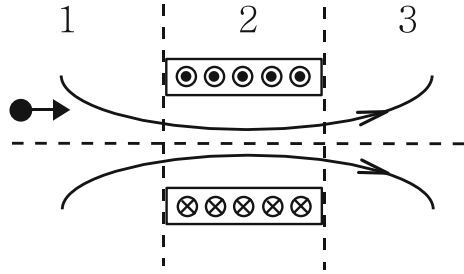


Fig. 7.13 Motion of an electron in a uniform solenoidal field as observed over two complete orbits in the laboratory frame (*left*) and in the Larmor frame (*right*)

Fig. 7.14 Fields of a solenoid divided into two fringe field regions and an interior region of approximately constant axial field



then act on to give focusing. The actual mechanism can be understood in terms of a three-stage process depicted in Fig. 7.14.

We divide the fields of the solenoid arbitrarily into three regions. In region 1, a charged particle moving parallel to the axis of the solenoid is acted upon by the *radial* component of the field giving rise to an *azimuthal* velocity. In the interior region (region 2), the situation is roughly what we have just investigated, a constant axial field. The azimuthal velocity is now acted upon by the axial field to produce a radial (focusing) force. As the particle leaves the solenoid in region 3, it encounters a radial field of opposite sign to that in region 1, which spins the particle back down, removing its azimuthal velocity. The particle then leaves the solenoid with a net kick towards the axis and no rotation.

Solenoids whose polarities alternate from one to the next can also be used to stably transport a beam and have certain advantages. Magnetic and electric quadrupoles can also be used to focus and guide beams. Magnetic quadrupoles have generally been employed only for downstream beamlines in electron induction linacs as described in detail in Chap. 8.

7.4 Envelope Equations

There are several types of envelope equations that can be found in the literature. One that is widely used in electron induction linacs is that due to Lee and Cooper [9]. It is an equation for the RMS (root mean square) radius of a cylindrically symmetric beam and is correct for arbitrary radial density profiles (since almost all induction linacs use solenoidal focusing the beam is generally cylindrically symmetric inside the accelerator).

7.4.1 Lee-Cooper Envelope Equation

We will sketch the derivation of this envelope equation. We start from the single particle equation of motion for a particle subjected to a radial force $F(r)$:

$$\gamma_b \beta^2 m_e c^2 \frac{\partial^2 \mathbf{r}}{\partial z^2} = F(r) \hat{\mathbf{e}}_r. \quad (7.37)$$

We now dot \mathbf{r} into this equation to get

$$\gamma_b \beta^2 m_e c^2 \mathbf{r} \cdot \frac{\partial^2 \mathbf{r}}{\partial z^2} = F(r)r. \quad (7.38)$$

Now

$$\mathbf{r} \cdot \frac{\partial^2 \mathbf{r}}{\partial z^2} = \frac{\partial^2}{\partial z^2} \left(\frac{\mathbf{r} \cdot \mathbf{r}}{2} \right) - \left(\frac{\partial \mathbf{r}}{\partial z} \right)^2, \quad (7.39)$$

so that Eq. (7.38) can be written as

$$\gamma_b \beta^2 m_e c^2 \left[\frac{\partial^2}{\partial z^2} \left(\frac{r^2}{2} \right) - \left(\frac{\partial \mathbf{r}}{\partial z} \right)^2 \right] = F(r)r. \quad (7.40)$$

We now average this equation over the beam profile. The average of r^2 is just the square of the RMS radius R . The second term in brackets in Eq. (7.40) is just the square of the total transverse velocity so that its average is the square of the RMS transverse velocity V (when using z as the independent variable we will often speak of a quantity such as $\partial x/\partial z$ as a *velocity* even though it is dimensionless and is in fact an angle). Performing the average yields

$$\gamma_b \beta^2 m_e c^2 \left[\frac{\partial^2}{\partial z^2} \left(\frac{R^2}{2} \right) - V^2 \right] = \overline{F(r)r}, \quad (7.41)$$

where the bar over the right hand side indicates an average over the beam. Expanding the second derivative gives (where a prime denotes differentiation with respect to z)

$$\gamma_b \beta^2 m_e c^2 (RR'' + R'^2 - V^2) = \overline{F(r)r}. \quad (7.42)$$

We can now write this as

$$R'' = \left(\frac{V^2 - R'^2}{R} \right) + \frac{\overline{F(r)r}}{\gamma_b \beta^2 m_e c^2 R}. \quad (7.43)$$

We must now define a quantity called the *emittance* which is a measure of the area in transverse phase space occupied by the beam (actually it is the area in transverse *trace* space $x-x'$ as opposed to phase space which is $x-p_x$). For a cylindrically symmetric beam the RMS emittance E is given by

$$E = R\theta_t, \quad (7.44)$$

where θ_t is the RMS random transverse velocity at a point where the beam has $R' = 0$. The quantity $\gamma\beta E$ is called the *normalized RMS emittance* and is constant if

the forces on the beam are linear in radius. When these forces are not linear, the emittance may grow and the envelope equation becomes less accurate as a computational tool to evaluate beam behavior.

The condition that the emittance is conserved implies that the external forces are linear in r and that the beam undergoes *self-similar* (profile preserving) radial motion. Under these assumptions, we may decompose the transverse velocity into a coherent part and a random residual part

$$\mathbf{V} = R' \frac{\mathbf{r}}{R} + \boldsymbol{\theta}_t. \quad (7.45)$$

Now if we square Eq. (7.45) and average over the beam, we obtain

$$V^2 = R'^2 + \theta_t^2 + 2 \frac{R'}{R} \overline{\mathbf{r} \cdot \boldsymbol{\theta}_t}. \quad (7.46)$$

The last term in Eq. (7.46) vanishes since it is the average of the radial component of the random velocity which has zero mean. Therefore, we have that

$$\theta_t^2 = V^2 - R'^2, \quad (7.47)$$

so that with the help of Eq. (7.44) we may write Eq. (7.43) as

$$R'' = \frac{E^2}{R^3} + \frac{\overline{F(r)r}}{\gamma_b \beta^2 m_e c^2 R}. \quad (7.48)$$

Equation (7.48) is a simplified form of the beam envelope equation. The force $F(r)$ in general includes the beam's own space charge fields and the external focusing force.

Let us consider the beam's space charge fields first. When viewed in the lab frame, the beam has a line charge density of $I(r)/\beta c$ which produces a radial electric field

$$E_r = \frac{I(r)}{2\pi\epsilon_0\beta cr}, \quad (7.49)$$

where $I(r)$ is the current enclosed as a function of radius.

Now the beam also appears in the lab frame as a moving current so that it produces an azimuthal component of magnetic field

$$B_\theta = \frac{\mu_0 I(r)}{2\pi r}. \quad (7.50)$$

The total (radial) Lorentz force on a charged particle in the beam is given by

$$F(r)_s = e[E_r - \beta c B_\theta] = e \left[\frac{I(r)}{2\pi\epsilon_0\beta cr} - \frac{\mu_0 I(r)\beta c}{2\pi r} \right] = \frac{eI(r)}{2\pi\epsilon_0\gamma_b^2\beta cr}, \quad (7.51)$$

where we have used the fact that $\gamma_b^{-2} = 1 - \beta^2$. The subscript s on the left hand side of Eq. (7.51) refers to the fact that we are computing the radial force due only to the beam's self fields. The net self force causes the beam to expand.

Let us now consider the average of $F(r)_{sr}$ over the beam:

$$\overline{F(r)_{sr}} = \frac{e\overline{I(r)}}{2\pi\epsilon_0\gamma_b^2\beta c}. \quad (7.52)$$

To compute the average over the beam of any quantity A , we use the prescription

$$\overline{A} = \frac{1}{I} \int_0^\infty 2\pi r J(r) A dr, \quad (7.53)$$

where $J(r)$ is the current density. This simply weights the quantity $A(r)$ by the amount of current near that radius and is the continuum analog of summing the quantity A_i for a beam particle over all the particles in the beam and dividing by the total number. But,

$$J(r) = \frac{1}{2\pi r} \frac{dI(r)}{dr}, \quad (7.54)$$

so that Eq. (7.52) can be written as

$$\overline{F(r)_{sr}} = \frac{e}{2\pi\epsilon_0\gamma_b^2\beta c I} \int_0^\infty I(r) \frac{dI(r)}{dr} dr = \frac{eI}{4\pi\epsilon_0\gamma_b^2\beta c}. \quad (7.55)$$

Using this result in Eq. (7.48) gives the envelope equation

$$R'' = \frac{E^2}{R^3} + \frac{I}{(\gamma_b\beta)^3 I_0 R} + \frac{\overline{F(r)_{fr}}}{\gamma_b\beta^2 m_e c^2 R} \quad (7.56)$$

where the quantity I_0 which has dimensions of current is

$$I_0 = \frac{4\pi\epsilon_0 m_e c^3}{e} \cong 17.1 \text{ kA}. \quad (7.57)$$

I_0 is related to the Alfvén current I_A by $I_A = \gamma\beta I_0$ which represents a limiting current where the beam's magnetic field bends the electrons backwards and inhibits propagation in vacuum [10]. The subscript f on $F(r)$ on the right hand side of Eq. (7.56) refers to the fact that now $F(r)$ is due to external focusing forces.

We have derived Eq. (7.56) under the assumption that γ was held constant. That restriction may be removed to produce a more general envelope equation capable of handling acceleration. When external focusing is present, it can be represented by a term proportional to R (this will be valid for solenoids or any other type of linear focusing system). The constant of proportionality is the square of the betatron

wavenumber which is the analog of the oscillation frequency in a mass-spring system. The betatron wavenumber is in general a function of z . Thus we may write

$$R'' + \frac{(\gamma_b \beta)'}{\gamma_b \beta} R' = \frac{E^2}{R^3} + \frac{I}{(\gamma_b \beta)^3 I_0 R} - k_\beta^2 R. \quad (7.58)$$

Equation (7.58) is the most general envelope equation for a cylindrically symmetric beam (without canonical angular momentum that is).

There are many interesting and useful solutions to Eq. (7.58). We will examine just one of these: the equilibrium radius of the beam in a solenoidal focusing field. The condition for equilibrium is

$$R'' = R' = 0. \quad (7.59)$$

The solution of Eq. (7.58) then becomes

$$R = \sqrt{\frac{2E}{k_c}} \left[\theta + \sqrt{\theta^2 + 1} \right]^{1/2}, \quad (7.60)$$

where the dimensionless quantity θ is given by

$$\theta \equiv \frac{I}{2(\gamma_b \beta)^3 I_0 k_c E}. \quad (7.61)$$

When θ is very large, the beam is said to be *space charge dominated* and the equilibrium radius asymptotes to

$$R = \sqrt{\frac{2I}{(\gamma_b \beta)^3 I_0 k_c^2}}. \quad (7.62)$$

When θ is very small, the beam is *emittance dominated* and the equilibrium radius becomes

$$R = \sqrt{\frac{2E}{k_c}}. \quad (7.63)$$

7.4.2 KV Envelope Equations

So far we have discussed an envelope equation which corresponds to the RMS quantities of a beam. Another envelope equation in wide use is that due to Kapchinskij and Vladimirskij [11]. The KV distribution is a delta function in the four dimensional transverse trace space of the beam and has the property that any two dimensional projection of this distribution is uniform. Thus a KV beam has uniform density in configuration space and produces linear self fields. This beam has a hard edge and the KV are used in the presence of quadrupole focusing.

If the situation is rotationally symmetric, these equations collapse to

$$R'' = \frac{E^2}{R^3} + \frac{2I}{(\gamma_b\beta)^3 I_0 R} - k_\beta^2 R, \quad (7.64)$$

where R and E now represent *edge* quantities [note the factor of 2 difference in the space charge term between this result and Eq. (7.58)].

7.5 Corkscrew Motion

An accelerator is never perfectly aligned. We will focus on the effects of chromatic aberration and misalignments of solenoidal focusing systems on the beam transverse motion in this section. An incoming beam misaligned with respect to the magnetic flux line will gyrate around the magnetic flux line regardless of whether the beam or the magnet is misaligned with respect to the machine axis. If the beam energy is constant within the pulse, the entire beam rotates at the same cyclotron frequency. Then, at any given z position along the machine, the beam is uniformly displaced in the transverse plane. However, if there is an energy variation within the beam pulse, the energy dependence of the cyclotron frequencies makes different slices of the beam rotate at different rates. These slices arrive at a downstream z position with different phase advances and different transverse displacements. The beam becomes twisted, and its centroid will progressively distort into a higher pitch helix as it travels downstream. If the difference in the phase advances among these slices are larger than 2π , the beam displacement of the entire beam pulse resembles a corkscrew. Hence, we call the transverse beam motion caused by chromatic aberrations and misalignments “corkscrew motion” [12–14]. Corkscrew-type oscillations can also be found in any linear focusing system, such as alternating gradient (AG) quadrupole transport systems. An initially straight beam in an AG system will develop wiggles whose frequency upshifts as the beam propagates.

7.5.1 Corkscrew Amplitude

If a magnet is misaligned with respect to the beam, the beam will experience an error dipole field component. For an offset δs_x in the x direction, the error field is approximately

$$\delta \mathbf{B}_x \approx -\frac{\delta s_x}{2} \left. \frac{\partial B_z(z, r)}{\partial z} \right|_{r=0} \hat{\mathbf{e}}_x, \quad (7.65)$$

as given by Eq. (7.13). For a tilt $\delta\theta_x$ in the x direction, the error field is approximately

$$\delta \mathbf{B}_x \approx \left[B_z + \frac{z - z_0}{2} \left. \frac{\partial B_z(z, r)}{\partial z} \right|_{r=0} \right] \delta\theta_x \hat{\mathbf{e}}_x. \quad (7.66)$$

For simplicity, we use phasors to represent the error field, the transverse displacement and the corkscrew amplitude in this section. The total error field of the focal system is $\delta B(z) = \Sigma \delta B_j(z)$, where

$$\delta B_j(z) = \delta B_{x,j}(z) + i\delta B_{y,j}(z), \quad (7.67)$$

and j is the index of the j -th misaligned solenoid. The displacement of the magnetic flux line of this solenoidal system is given by

$$\Delta(z) = \int_0^z \frac{\delta B(z')}{B_z} dz'. \quad (7.68)$$

Assuming no acceleration, the equation of motion for the beam is

$$\xi'' - ik_c \xi' = -ik_c \frac{\delta B}{B_z}, \quad (7.69)$$

where $\xi = x + iy$. Assume that the beam is perfectly aligned at the beginning of the accelerator, i.e., $\xi = 0$ and $\xi' = 0$. Then, the beam slice at location z rotates around the displaced flux line $\Delta(z)$ with a gyro-radius $|\rho(z, \tau)|$ as shown in Fig. 7.15 and its transverse displacement $\xi(z, \tau)$ is given by

$$\xi(z, \tau) = \Delta(z) - \rho(z, \tau)e^{ik_c(\tau)z}, \quad (7.70)$$

where

$$\begin{aligned} \rho(z, \tau) &= \int_0^z \frac{\delta B(z')}{B_z} e^{-ik_c(\tau)z'} dz' \\ &= \sum_{j=1}^n \int_0^z \frac{\delta B_j(z')}{B_z} e^{-ik_c(\tau)z'} dz', \end{aligned} \quad (7.71)$$

n is the index of the last magnet within distance z , and $k_c(\tau)$ is the cyclotron wavenumber. Since the error field usually is localized around the misaligned magnet

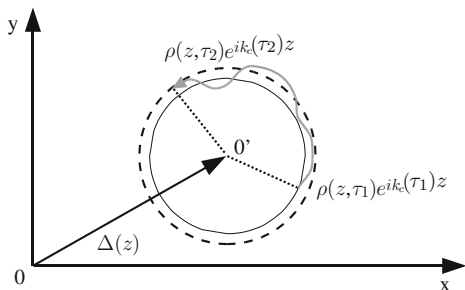


Fig. 7.15 Beam centroid gyrates around an offset magnetic flux line. Beam slices with different energies have different gyro-radii and phases

location, we can extend the above integration range to $(-\infty, \infty)$ and rewrite the above equation as

$$\rho(z, \tau) = \sum_{j=0}^n \frac{\delta \tilde{B}_j(\tau)}{B_z}, \quad (7.72)$$

where

$$\delta \tilde{B}_j = \int_{-\infty}^{\infty} \delta B_j(z') e^{-ik_c(\tau)z'} dz', \quad (7.73)$$

is the Fourier component of the j th error field at the cyclotron wavenumber. For a beam having an energy variation over its length, different beam slices rotate at different cyclotron wavenumbers with different gyro-radii as the beam propagates in the solenoidal system. The differential gyration within the beam pulse is called corkscrew motion, and its amplitude is given as

$$\eta(z, \tau) = \langle \rho(z, \tau) e^{ik_c(\tau)z} \rangle - \rho(z, \tau) e^{ik_c(\tau)z}, \quad (7.74)$$

where $\langle \rangle$ denotes time averaging over the beam pulse. The time averaged corkscrew amplitude $A(z)$ is given as

$$A(z) = \langle \rho(z, \tau) \rho^*(z, \tau) \rangle^{1/2}. \quad (7.75)$$

The phase of the beam gyration is accumulated from the misaligned magnets' origin. When the differential phase advance $\delta k_c(\tau)z$ within the pulse is much less than 1, the corkscrew amplitude is roughly a linear function of the energy variation $\delta\gamma$, i.e.,

$$\eta(z, \tau) = \delta k_c(\tau)z \left[-i\rho(z, \tau_0) + \frac{1}{z} \frac{\partial \rho(z, \tau)}{\partial k_c} \Big|_{\tau_0} \right] e^{ik_c(\tau_0)z}, \quad (7.76)$$

and the time averaged corkscrew amplitude is given by

$$A(z) = \langle \delta k_c^2(\tau) \rangle^{1/2} z |\rho(z, \tau_0)| \left| 1 - \frac{1}{z} \frac{\partial \rho(z, \tau) / \partial k_c}{\rho(z, \tau)} \Big|_{\tau_0} \right|. \quad (7.77)$$

The second terms in Eqs. (7.76) and (7.77) are usually much smaller than the first terms since the Fourier spectrum of the error field is relatively flat around the cyclotron wavenumber. Hence, the corkscrew amplitude also increases linearly in z when the relative phase advance is small.

After the beam has traveled some distance, the relative phase advance is greater than 2π . The beam will resemble a corkscrew. The corkscrew motion is then "fully developed" with the gyro-radius as its amplitude, i.e.,

$$\eta(z, \tau_0) \cong -\rho(z, \tau) e^{i\delta k_c(\tau)z}, \quad (7.78)$$

and the time averaged corkscrew amplitude is given by

$$A(z) \cong |\rho(z, \tau_0)| \left[1 + \frac{1}{2} \left| \frac{\partial \rho(z, \tau)}{\partial k_c} \right|_{\tau_0} \langle \delta k_c^2(\tau) \rangle^{1/2} \right]. \quad (7.79)$$

Generally, the error field δB is linearly proportional to the focusing strength B_z so that changing the focusing field will not change the Fourier spectrum of $\delta B/B_z$ while the cyclotron wavenumber changing linearly with B_z may result in different gyro-radius. If the system has random error fields like white noise, the gyro-radius would be constant regardless of the focusing field strength. Then, according to Eqs. (7.76) and (7.77), the corkscrew amplitude also increases linearly in B_z when the differential phase advance within the pulse is much less than 1. However, it is noteworthy that Eqs. (7.78) and (7.79) indicate that the amplitude of a fully developed corkscrew motion may not change when the focusing solenoids' strength is changed.

7.5.2 Tuning Curve Algorithm

The corkscrew motion is caused by misalignment of the system and energy variation within the beam pulse. Intuitively, one would try to reduce the magnetic flux line's transverse displacement to minimize the corkscrew motion within a beam pulse with a given energy variation. However, this method does not always reduce corkscrew amplitude. Reducing the transverse displacement of the magnetic flux line only guarantees reduction of the DC component of the error field or the z -averaged error field. Since the corkscrew amplitude depends on the Fourier component of the error field at the cyclotron wavenumber $k_c(t)$, to remove the corkscrew motion, we have to remove the Fourier component of the error field at the cyclotron wavenumber $k_c(t)$ instead.

To begin the beam steering during accelerator operation, the focusing magnet should be set to produce a chosen magnetic profile for the target beam quality. The steering procedure can be incorporated into a computerized data acquisition and control system, such as the MAESTRO [14] program used on the ETA-II. The control system acquires and processes signals from the beam position monitors. The beam displacements $x(z, t)$ and $y(z, t)$ are recorded as functions of time t at the beam position monitors. The beam centroid position over the pulse t_1 to t_2 is given by $(\langle x(z, t) \rangle, \langle y(z, t) \rangle)$. The corkscrew amplitude $\eta(z, t)$ is calculated as

$$\eta(z, t) = [x(z, t) - \langle x(z, t) \rangle] + i[y(z, t) - \langle y(z, t) \rangle], \quad (7.80)$$

and the time averaged corkscrew amplitude is calculated as

$$A(z) = \left\langle [x(z, t) - \langle x(z, t) \rangle]^2 + i[y(z, t) - \langle y(z, t) \rangle]^2 \right\rangle^{1/2}. \quad (7.81)$$

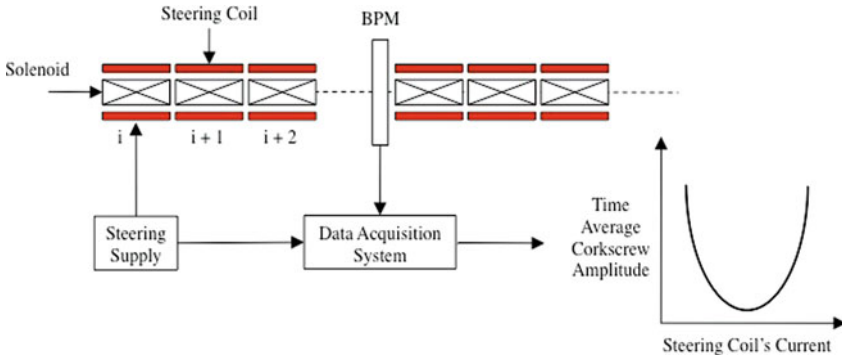


Fig. 7.16 The time-independent, dynamic beam steering algorithm reduces the corkscrew amplitude by minimizing the time averaged corkscrew amplitude

Since the corkscrew amplitude is the differential beam displacement from the averaged centroid position, the offset of the beam position monitor will not be included in the calculated corkscrew amplitude. Therefore, the time-averaged corkscrew amplitude calculated by the control system is only determined by the net error field that includes both the alignment error field and the steering field. Varying the excitation current on a steering magnet will change the magnitude of the time averaged corkscrew amplitude $A(z)$. We will obtain a well-defined minimum $A(z)$ while tuning the steering coils current to its optimal setting. Operationally the accelerator is steered iteratively, starting at the injector and sequentially adjusting a chosen steering coils current for a minimum in the time averaged corkscrew amplitude observed by a downstream beam position monitor until the end of the accelerator is reached (see Fig. 7.16). When the alignment errors are large, repeating the steering process for the whole accelerator may be needed to reach convergent settings on the steering coils.

Note that the corkscrew motion is removed when the Fourier component of the steering field at the cyclotron wavenumber cancels out the error field's Fourier component at k_c . Therefore, one can minimize the corkscrew amplitude on the BPM at the end of the accelerator while using only one pair of steering coils at the beginning of the accelerator if the steering supply can supply infinite amount of steering current, and if the displacement in the middle of the accelerator is not an issue.

Figure 7.17 shows the corkscrew motion observed on the ETA-II accelerator. For the 20-cell experiments, two beam position monitors are located at the end of the 20 cells [15]. The unsteered corkscrew amplitude was about 8 mm (see Fig. 7.17a). When the steering coils were used to straighten the magnetic flux line by using the Stretched Wire Alignment Technique (SWAT) [16–21], i.e., the DC component of the error field was minimized. The observed corkscrew amplitude was only reduced slightly from 8 to 6 mm (see Fig. 7.17b). Finally, we steered the beam by implementing the corkscrew tuning curve steering algorithm. The observed corkscrew tuning curves for all the steering coils had the shape of “V” with well-defined

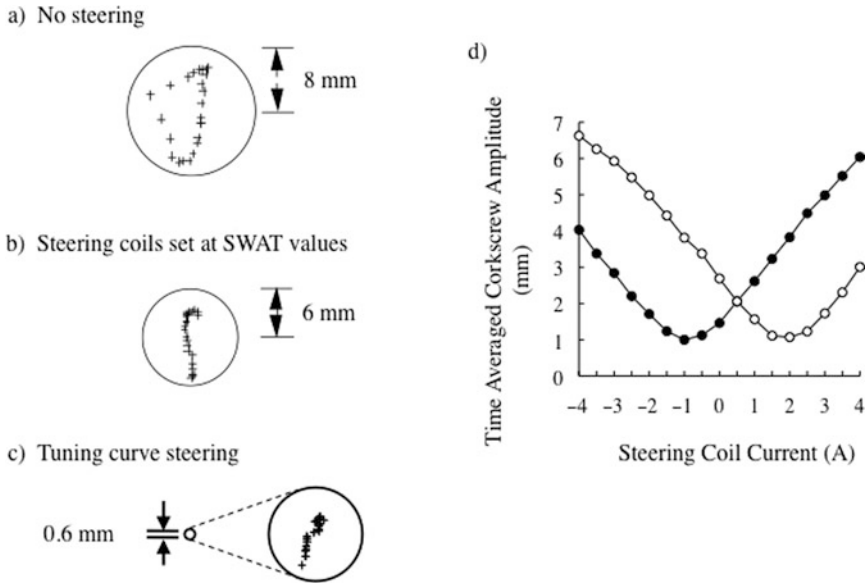


Fig. 7.17 Measured beam displacement for 40 ns on a 20-cell ETA-II experiment with (a) no steering, (b) correction of tilts by using SWAT values, (c) the corkscrew tuning curve steering algorithm, and (d) observed ETA-II corkscrew tuning curves for the horizontal and the vertical steering coils at the last injector cell [16]

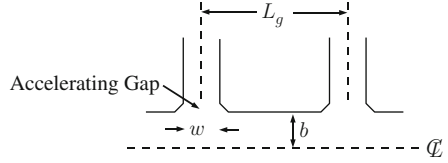
minimums, and that for the steering coil pair at the last injector cell are shown in Fig. 7.17d. We had observed one order of magnitude reduction on the 20-cell ETA-II's corkscrew amplitude, and the final corkscrew amplitude was reduced to 0.6 mm (see Fig. 7.17c). A similar corkscrew amplitude reduction was also achieved on the FXR accelerator by using this tuning algorithm [22, 23].

7.6 Instabilities

7.6.1 Image Displacement Instability

Both instabilities to be discussed in this section depend on the beam current. This is a parametric instability and arises because an offset beam is subjected to a periodic defocusing force at each accelerating gap. This force arises from the lack of cancellation of the electric and magnetic image forces at the gap [24, 25]. The presence of the gap nearly eliminates the restoring force to the beam centroid provided by the image current. The gap, however, only minimally perturbs the destabilizing force from the image charge. The model geometry is shown in Fig. 7.18. We will assume that the image current forces are absent over the gap while the image charge forces are unperturbed from their smooth pipe value. We can then Fourier analyze the spatial dependence of this force and define a gap

Fig. 7.18 Periodic-gap geometry for image displacement and BBU calculations is shown



occupation function $g(z)$. In terms of this function, the equation of motion for the centroid is

$$\xi'' - ik_c \xi' - p^2 g(z) \xi = 0. \quad (7.82)$$

We remove the first derivative term as we did in Sect. 7.3.3 by defining $\xi = \Omega e^{ik_c z/2}$. Then we obtain

$$\Omega'' + \frac{k_c^2}{4} \Omega - p^2 g(z) \Omega = 0, \quad (7.83)$$

where p^2 is given by

$$p^2 = \frac{2I}{\gamma \beta^3 I_0 b^2}. \quad (7.84)$$

Here $g(z)$ is given by

$$g(z) = \frac{w}{L_g} + \frac{2}{\pi} \sum_{n=1}^{\infty} \frac{1}{n} \sin\left(\frac{n\pi w}{L_g}\right) \cos\left(\frac{2\pi n z}{L_g}\right). \quad (7.85)$$

If we retain the first two terms in the expansion for $g(z)$, we will obtain the *Mathieu equation*

$$\Omega'' + \left[\frac{k_c^2}{4} - k^2 - \frac{2p^2}{\pi} \sin\left(\frac{\pi w}{L_g}\right) \cos\left(\frac{2\pi z}{L_g}\right) \right] \Omega = 0, \quad (7.86)$$

where k^2 is given by

$$k^2 = \frac{2Iw}{\gamma \beta^3 I_0 b^2 L_g}. \quad (7.87)$$

Here L_g is the distance between gaps, w is the effective gap width, and b is the pipe radius. By defining $\zeta = 2\pi z/L_g$, we may cast this equation into a standard form

$$\frac{\partial^2 \Omega}{\partial \zeta^2} + [a - 2\epsilon \cos(\zeta)] \Omega = 0, \quad (7.88)$$

with a and ϵ given by

$$a = \frac{L_g^2}{4\pi^2} \left[\frac{k_c^2}{4} - k^2 \right], \tag{7.89}$$

$$\epsilon = \frac{p^2 L_g^2}{2\pi^3} \sin\left(\frac{\pi w}{L_g}\right). \tag{7.90}$$

The solutions to Eq. (7.88) may be stable or unstable depending on the values of a and ϵ . A plot of the boundaries between stable and unstable solutions is shown in Fig. 7.19. The shaded regions are stable. An approximation for the shape of the stability boundary between $a = 0$ and $a = 1/4$ is given by

$$a(\epsilon) = \frac{1}{4} - \epsilon - \frac{\epsilon^2}{2}. \tag{7.91}$$

Applying this condition for the first stability region $0 \leq a \leq 1/4$ requires

$$\epsilon < \sqrt{\frac{3}{2} - 2a} - 1. \tag{7.92}$$

Note that $k_c^2 \sim \gamma^{-2}$ while $k^2 \sim \gamma^{-1}$ so that if the solenoidal field strength is not increased with acceleration to higher energies eventually $a(\epsilon)$ will become negative and the beam motion will become unstable. At that point, the average defocusing force of the gaps will be stronger than the applied focusing.

This instability can be of concern for very high current machines where some novel accelerating cell geometries have been developed to minimize both the image displacement effect and the Beam Breakup Instability [26]. The constraints imposed upon accelerator design and magnetic field tune by the image displacement force are further discussed in Sect. 7.7.1.

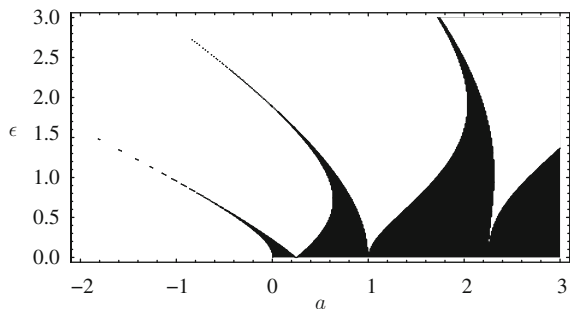


Fig. 7.19 Stability boundaries of the Mathieu equation. The dark regions are stable

7.6.2 Beam Breakup Instability (BBU)

This is perhaps the most serious instability for a long, high current linac and sets the focusing requirements and current limit for the machine (an exception may occur for high current, heavy ion linacs where the focusing required to confine the beam against its own space charge forces may be a more demanding requirement than suppressing BBU). Historically, the instability was discovered circa 1957 but gained prominence when SLAC was turned on. As initially designed, SLAC had only ~ 10 betatron wavelengths for the entire 2 mile accelerator. The appearance of BBU necessitated the installation of extra quadrupoles to limit the number of e-folds of growth [27].

The instability arises from the beam interacting with the dipole TM modes of the accelerating cavities. These modes have z -components of electric field that extract energy from the beam and have transverse magnetic fields that act to deflect the beam. In most high current linacs the accelerating cavities are far enough apart that electromagnetic fields from one cell do not appreciably excite modes in adjacent cells. This leads to what is termed *cumulative* BBU where there are only local interactions between the cavities and the beam.

7.6.2.1 Continuous System Model

We will treat a set of model equations for the instability that approximates the accelerator structure as a continuous system. This requires that there be many gaps per betatron wavelength. Any phenomena that depend upon the periodic spacing of the cavities will be lost in this model, but it yields the most important features of the instability. In addition, we will assume continuous solenoidal focusing although the method and the results can be easily extended to any type of smoothed focusing system.

In general, there will be many dipole RF modes. When the beam passes by the accelerator gap, it will experience a transverse Lorentz force from the mode magnetic field. This force will result in a change in transverse momentum of the beam. Let us define Δ as the average change in angle of the beam per unit length

$$\begin{aligned} \Delta &\equiv \frac{\Delta p_x + i \Delta p_y}{p_z L_g} \\ &= -\frac{e}{\gamma_b \beta m_e c} \int_{\text{gap}} (\hat{\mathbf{e}}_x \cdot \beta c \hat{\mathbf{e}}_z \times \hat{\mathbf{e}}_y B_y + i \hat{\mathbf{e}}_y \cdot \beta c \hat{\mathbf{e}}_z \times \hat{\mathbf{e}}_x B_x) \left(\frac{dz}{\beta c} \right). \end{aligned} \quad (7.93)$$

From now on, we will take $\beta = 1$. The dipole modes in the cell are in turn excited by the transverse beam oscillations as described in Sect. 6.10.1. With a beam displacement ξ varying as $\exp(i\omega t)$ the frequency dependent response of the cell can be characterized by the transverse interaction impedance discussed in Sect. 6.10. Using the definition of transverse impedance in Eq. (6.29), the change

in angle per unit length can be related to the beam centroid oscillation amplitude as [28, 29]

$$\Delta = -\frac{ieZ_t(\omega)I}{L_g\gamma_b m_e c^2} \xi. \quad (7.94)$$

We now complete the set of model equations by writing the equation of motion for the beam centroid

$$\frac{\partial}{\partial z} \left(\gamma_b \frac{\partial \xi}{\partial z} \right) - i\gamma_b k_c \frac{\partial \xi}{\partial z} = \gamma_b \Delta, \quad (7.95)$$

where we have explicitly allowed for acceleration and variable focusing strength. A detailed analysis of the general case with varying energy and focusing strength is presented in the following Section, assuming a single high Q mode. Here we derive a useful scaling law for the instability growth rate by considering the dispersion equation of a uniform system (constant focusing strength and constant beam energy). With a beam centroid displacement of the form

$$\xi \sim \exp(i\omega\tau - ikz) \quad (7.96)$$

from Eqs. (7.94) and (7.95) we have the following solution for the wavenumber $k(\omega)$

$$k(\omega) = -\frac{k_c}{2} \pm \left[\frac{k_c^2}{4} + iA(\omega) \right]^{1/2} \quad (7.97)$$

where

$$A(\omega) = \frac{eZ_t(\omega)I}{L_g\gamma_b m_e c^2}. \quad (7.98)$$

It is easy to show that the instability is convective in the lab frame [30], so the amplification over a distance z as a function of the excitation frequency can be computed from $\text{Im}(k)$ at $\text{Re}(\omega)$. In most cases of interest, the focusing strength is strong enough to make

$$A \ll \frac{k_c^2}{4} \quad (7.99)$$

In this case, the amplification after N accelerator cells ($N = z/L_g$), is

$$\xi \sim \exp \left[\frac{NI}{B_0 c} \text{Re}(Z_t(\omega)) \right]. \quad (7.100)$$

7.6.2.2 Instability Growth with a Single High Q Mode

If we take the single mode model, we can express the transverse impedance as

$$Z_t(\omega) = \frac{i\omega_0^3(Z_\perp/Q)/c}{\omega_0^2 - \omega^2 + i\omega\omega_0/Q}. \tag{7.101}$$

The parameter Z_\perp/Q is called the transverse shunt impedance of the mode and determines the degree to which the mode is excited by the beam. The real and imaginary parts of the impedance are plotted in Fig. 7.20. The real part is responsible for BBU as we have shown. The value of the imaginary part of Z_t at zero frequency is responsible for the image displacement force. The actual impedance will be the sum of the contributions from all of the RF dipole modes in the cell. If the modes are well separated, the peaks of the real part will be almost unaffected by the presence of the other modes. However, all the modes will contribute to the value of the imaginary part at zero frequency.

We consider an initial value problem to obtain the asymptotic growth rate, and use the Laplace transform notation $s = i\omega$. If the cavities are quiescent when the head of the beam passes by, motion of the beam centroid is given by

$$\frac{\partial^2 \tilde{\xi}}{\partial z^2} + \left(\frac{1}{\gamma_b} \frac{\partial \gamma}{\partial z} - ik_c \right) \frac{\partial \tilde{\xi}}{\partial z} - \frac{h(s)}{\gamma_b} \tilde{\xi} = 0, \tag{7.102}$$

where a tilde denotes the Laplace transform and the function $h(s)$ is

$$h(s) = \frac{\omega_0^2 G}{s^2 + \frac{\omega_0}{Q}s + \omega_0^2}. \tag{7.103}$$

Here the quantity G is given by

$$G = \frac{4\pi\epsilon_0\omega_0}{L_g} \frac{I}{I_0} \left(\frac{Z_\perp}{Q} \right). \tag{7.104}$$

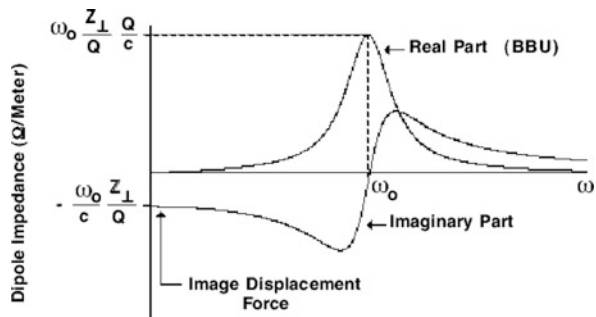


Fig. 7.20 Single mode dipole cell impedance for $Q = 4$

We proceed to remove the first derivative terms by defining

$$\tilde{\xi} = \frac{\tilde{\Omega}}{\sqrt{\gamma_b}} \exp \left\{ \frac{i}{2} \int_0^z k_c dz' \right\}. \quad (7.105)$$

Substitution into Eq. (7.102) yields

$$\frac{\partial^2 \tilde{\Omega}}{\partial z^2} + \left[\frac{k_c^2}{4} - \frac{h(s)}{\gamma_b} + \frac{i}{2} \frac{\partial k_c}{\partial z} - \frac{1}{2\gamma_b} \frac{\partial^2 \gamma}{\partial z^2} + \frac{1}{4\gamma_b^2} \left(\frac{\partial \gamma}{\partial z} \right)^2 + \frac{ik_c}{\gamma_b} \frac{\partial \gamma}{\partial z} \right] \tilde{\Omega} = 0. \quad (7.106)$$

We now consider the case of uniform acceleration and put

$$\gamma_b = \gamma_0 + \lambda z. \quad (7.107)$$

We now assume that k_c changes very little in a cyclotron wavelength, i.e. that $k_c^2 \gg k'_c$ and also that $k_c \gg \lambda/\gamma_b$. Then, Eq. (7.106) becomes

$$\frac{\partial^2 \tilde{\Omega}}{\partial z^2} + \left[\frac{k_c^2}{4} - \frac{h(s)}{\gamma_b} \right] \tilde{\Omega} \cong 0, \quad (7.108)$$

which has the WKB solution

$$\tilde{\Omega} \approx \frac{A(s)}{\left[\frac{k_c^2}{4} - \frac{h(s)}{\gamma_b} \right]^{1/4}} \exp \left\{ i \int_0^z \left[\frac{k_c^2}{4} - \frac{h(s)}{\gamma_b} \right]^{1/2} dz' \right\} + \text{c.c.} \quad (7.109)$$

Let us consider a beam that is injected into the accelerator with an aiming error but with no initial displacement. Then $\xi(0, \tau) = 0$ and $\xi'(0, \tau) = \xi'_0$, and we find that

$$\tilde{\xi}(z, s) = \frac{\xi'_0}{s} \sqrt{\gamma_0} \frac{\exp \left\{ \frac{i}{2} \int_0^z k_c dz' \right\}}{\left[\frac{k_c^2(0)}{4} - \frac{h(s)}{\gamma_0} \right]^{1/4} \left[\frac{k_c^2}{4} - \frac{h(s)}{\gamma_b} \right]^{1/4}} \sin \left\{ \int_0^z \left[\frac{k_c^2}{4} - \frac{h(s)}{\gamma_b} \right]^{1/2} dz' \right\}. \quad (7.110)$$

In order to somewhat simplify Eq. (7.110) we will make the *strong focusing* approximation. Specifically, we require

$$\frac{k_c^2}{4} \gg \frac{h(s)}{\gamma_b}. \quad (7.111)$$

We will see later that this is satisfied if $\frac{k_c^2}{4} \gg \frac{GQ}{\gamma_b}$. We use this condition to neglect $h(s)$ in the denominator of Eq. (7.110) while we expand the radical in the exponent

and keep the first term in $h(s)$. It is this term that will yield the asymptotic growth rate. We define $\phi(z)$ and $\Gamma(z)$ as

$$\phi(z) = \int_0^z k_c dz', \quad (7.112)$$

$$\Gamma(z) = \int_0^z \frac{dz'}{\gamma_b k_c}. \quad (7.113)$$

Then we may write Eq. (7.110) as

$$\tilde{\xi}(z, s) \approx \frac{\xi'_0}{ik_c(0)s} \sqrt{\frac{\gamma_0 k_c(0)}{\gamma k_c}} [e^{i\phi(z) - ih(s)\Gamma(z)} - e^{ih(s)\Gamma(z)}]. \quad (7.114)$$

In order to obtain the inverse Laplace transform of Eq. (7.114), we must compute integrals of the form

$$I_{\pm} \equiv \frac{1}{2\pi i} \int_{c-i\infty}^{c+i\infty} \frac{ds}{s} e^{s\tau \pm ih(s)\Gamma(z)}, \quad (7.115)$$

where the contour is taken to the right of all the singularities of the integrand. Consider the exponent of Eq. (7.115):

$$\Lambda_{\pm} = s\tau \pm ih(s)\Gamma(z). \quad (7.116)$$

Let us define a dimensionless variable σ and θ such that

$$s = \omega_0 \sigma, \quad (7.117)$$

and

$$\theta = \frac{\omega_0 \tau}{G\Gamma(z)}. \quad (7.118)$$

With these definitions Λ_{\pm} becomes

$$\Lambda_{\pm} = G\Gamma(z)\chi_{\pm} = G\Gamma(z) \left[\theta\sigma \pm \frac{i}{\sigma^2 + \frac{\sigma}{Q} + 1} \right], \quad (7.119)$$

and I_{\pm} becomes

$$I_{\pm} = \frac{1}{2\pi i} \int_{c-i\infty}^{c+i\infty} \frac{d\sigma}{\sigma} e^{G\Gamma(z)\chi_{\pm}(\sigma)}. \quad (7.120)$$

We will evaluate these integrals by the saddle point method. The asymptotic solution resulting from this procedure will become increasingly valid as $G\Gamma$ gets larger. The saddle points are found from solutions of

$$\frac{\partial \chi_{\pm}}{\partial \sigma} = \theta - \frac{(\pm i) \left(2\sigma + \frac{1}{Q}\right)}{\left(\sigma^2 + \frac{\sigma}{Q} + 1\right)^2} = 0. \quad (7.121)$$

There are two limiting cases corresponding to $\theta \ll 1$ and $\theta \gg 1$.

7.6.2.3 Long-Pulse BBU

Now we consider the important and interesting case $\theta \gg 1$. In order to satisfy Eq. (7.121) we must have $\sigma^2 + \sigma/Q + 1 \rightarrow 1$, i.e. σ must be close to the resonant frequency. So σ is approximately

$$\sigma \cong -\frac{1}{2Q} \pm i, \quad (7.122)$$

where we have neglected terms of order $1/Q^2$. At this point we do not know which sign to choose in Eq. (7.122). We now substitute into Eq. (7.121) to obtain

$$\left(\sigma^2 + \frac{\sigma}{Q} + 1\right)^2 \sim \frac{(\pm i)(\pm 2i)}{\theta} = \pm \frac{2}{\theta}. \quad (7.123)$$

The solutions to this equation give the saddle points. It turns out that the dominant contributions will come from the saddle points with an overall minus sign in Eq. (7.123). One can verify this by solving for the saddle points and then inserting them into the expression for χ_{\pm} and looking for the largest real part. Thus the dominant saddles are found as

$$\begin{aligned} \sigma_{0+} &\approx -\frac{1}{2Q} + i + \frac{1}{\sqrt{2\theta}}, \\ \sigma_{0-} &\approx -\frac{1}{2Q} - i + \frac{1}{\sqrt{2\theta}}. \end{aligned} \quad (7.124)$$

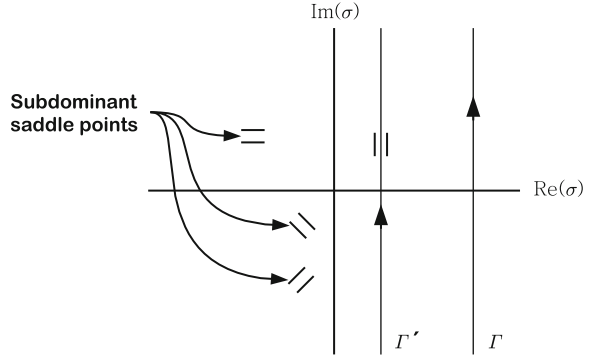
If $\theta < 2Q^2$, the dominant saddle points will lie to the right of the imaginary axis and there will be no contribution from the pole at the origin. If $\theta > 2Q^2$, the saddle points will lie to the left of the imaginary axis and there will be a contribution from the pole to the integrals in Eq. (7.120), but the saddle point contributions will dominate. These choices give

$$\chi_{\pm}(\sigma_0) \approx \pm i\theta - \frac{\theta}{2Q} + \sqrt{2\theta}. \quad (7.125)$$

and

$$\frac{1}{2} \frac{\partial^2 \chi_{\pm}(\sigma_0)}{\partial \sigma^2} \approx 2 \left(\frac{\theta}{2}\right)^{3/2}. \quad (7.126)$$

Fig. 7.21 Complex σ plane for I_+



We see from Eq. (7.126) that the steepest descent paths are vertical in the complex σ plane as shown in Fig. 7.21 (i.e., if we put $\sigma - \sigma_0 = \eta e^{i\lambda}$, we will find that $\lambda = \pi/2$). We now have all the pieces needed to assemble the solution

$$\xi(z, \tau) \sim \frac{\xi'_0}{k_c(0)} \sqrt{\frac{\gamma_0 k_c(0)}{\gamma_b k_c(z)}} \frac{e^{i\phi/2}}{2\sqrt{\pi G\Gamma}} \left(\frac{2}{\theta}\right)^{3/4} e^{G\Gamma(-\frac{\theta}{2Q} + \sqrt{2\theta})} \cos\left(\frac{\phi}{2} - \omega_0\tau\right), \quad (7.127)$$

where the magnitude of the growth is given by

$$|\xi(z, \tau)| \sim \frac{|\xi'_0|}{2\sqrt{\pi G\Gamma k_c(0)}} \sqrt{\frac{\gamma_0 k_c(0)}{\gamma_b k_c(z)}} \left(\frac{2}{\theta}\right)^{3/4} e^{G\Gamma(-\frac{\theta}{2Q} + \sqrt{2\theta})}. \quad (7.128)$$

Let us write out the exponential term in the growth formula:

$$G\Gamma \text{Re}(\chi) = -\frac{\omega_0\tau}{2Q} + \sqrt{2\omega_0\tau G\Gamma}. \quad (7.129)$$

Examination of this equation reveals that there is unique time τ_p for which the exponent is a maximum. For late times, the growth is damped by the losses in the cavities. Differentiating Eq. (7.129) and equating the result to zero yields τ_p as

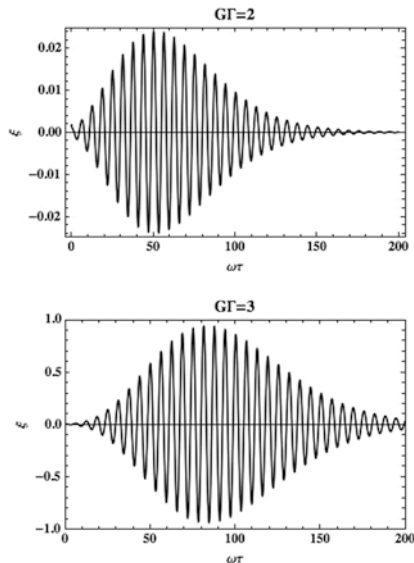
$$\omega_0\tau_p = 2Q^2 G\Gamma. \quad (7.130)$$

The location of the peak growth in the pulse moves further back towards the pulse tail as the beam propagates down the accelerator (increasing Γ). This is an example of a *convective* instability. Eventually the peak of the growth will propagate out the tail of the pulse leaving behind a growth envelope that is monotonically increasing from head to tail.

The value of the exponent, which occurs at τ_p , is

$$G\Gamma \text{Re}(\chi)_{\max} = GQ\Gamma, \quad (7.131)$$

Fig. 7.22 Convective behavior of long-pulse BBU



and the maximum magnitude of the growth is

$$|\xi(z, \tau)| \sim \frac{|\xi'_0|}{2\sqrt{\pi G\Gamma k_c(0)}} \sqrt{\frac{\gamma_0 k_c(0)}{\gamma_b k_c(z)}} \frac{e^{GQ\Gamma}}{Q^{3/2}}. \quad (7.132)$$

Figure 7.22 shows the value of $|\xi|$ versus τ at two different values of $G\Gamma$ that correspond to two different axial positions down the accelerator. The rapid oscillations are occurring at the frequency of the RF mode. Note the scale change between the two plots.

The maximum exponent, Eq. (7.131), has different functional forms depending on the focusing scheme used. The equation turns out to be correct for any type of smooth linear focusing if we just replace k_c by $2k_\beta$. For a constant field with or without acceleration, we have

$$k_\beta = \frac{k_0}{\gamma_b} \rightarrow \Gamma = \frac{z}{2\gamma_b k_\beta}, \quad (7.133)$$

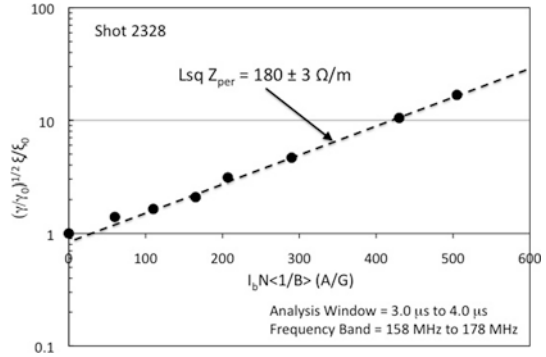
while if the field is ramped as $\sqrt{\gamma_b}$, we have

$$k_\beta = \frac{k_0}{\sqrt{\gamma_b}} \rightarrow \Gamma = \frac{\sqrt{\gamma_b} - \sqrt{\gamma_0}}{\lambda k_0}. \quad (7.134)$$

Finally, if the field is ramped proportionally to γ_b , we have

$$k_\beta = k_0 \rightarrow \Gamma = \frac{1}{2\lambda k_0} \log\left(\frac{\gamma_b}{\gamma_0}\right). \quad (7.135)$$

Fig. 7.23 BBU growth versus $GQ\Gamma$ in the DARHT-II accelerator is shown on a semi-log scale showing the exponential growth [31]



The parameter GQ that appears in the growth exponent is proportional to the product of all three RF mode parameters $\omega_0(Z_{\perp}/Q)Q$, which we can recognize as the peak of the resistive part of the transverse impedance for the single pole model (Eq. 7.101). Indeed, the e-folding rate in Eq. (7.133) for the case of a uniform focusing field is the same as Eq. (7.100).

The growth of BBU versus distance is shown for the DARHT-II machine in Fig. 7.23 [31]. Note that the measurements performed correspond to BBU growth due to the low frequency peak of the mode spectrum shown in Fig. 6.12. The growth is indeed exponential as expected and the inferred transverse impedance (from the BBU growth) is very close to the value determined by the technique described in Sect. 6.10.3.

7.7 Induction Linac Design Considerations

7.7.1 Optimal Focusing Strategy

The output beam of a high current accelerator may be required to drive a free electron laser or other device with a high energy selectivity. A typical requirement for a variety of applications of these beams is that the energy variation across the useful portion of the pulse (generally called the “flat top”) needs to be no larger than a few percent. This relatively small energy variation raises the possibility that practical machines could be constructed such that $\omega_s \tau_p \ll 1$. An obvious way to satisfy this criterion is to use a weak focusing field. However, a weak focusing field will invite BBU growth. We will shortly see that there is a unique way to grade the focusing strength so as to minimize the phase advance of a machine for a given level of BBU growth [32].

Let us recall that the number of e -folds of BBU in the long-pulse limit (the regime of operation of most high current linacs) is

$$\text{Re}(\Lambda) = GQ\Gamma = GQ \int_0^z \frac{dz'}{2\gamma_b k_{\beta}}. \quad (7.136)$$

We also need the betatron phase advance:

$$\phi_\beta = \int_0^z k_\beta dz'. \quad (7.137)$$

We take the case of constant average acceleration

$$\gamma_b(z) = \gamma_0 + \lambda z. \quad (7.138)$$

Then we may express Eqs. (7.136) and (7.137) as integrals over γ :

$$\text{Re}(\Lambda) = GQ\Gamma = \frac{GQ}{2\lambda} \int_{\gamma_0}^{\gamma_\infty} \frac{d\gamma'}{\gamma' k_\beta(\gamma')}, \quad (7.139)$$

$$\phi_\beta = \frac{1}{\lambda} \int_{\gamma_0}^{\gamma_\infty} k_\beta(\gamma') d\gamma', \quad (7.140)$$

where γ_∞ is the value of γ at the end of the accelerator.

The problem now is to minimize (7.140) subject to the constraint Eq. (7.139). That is, we wish to specify a fixed number of e -folds of BBU growth and find the functional form of $k_\beta(\gamma)$ that minimizes the betatron phase advance. To solve this problem, we minimize the auxiliary integral

$$\phi_\beta = \frac{1}{\lambda} \int_{\gamma_0}^{\gamma_\infty} \left[k_\beta(\gamma') + \frac{\mu GQ}{2\gamma' k_\beta(\gamma')} \right] d\gamma', \quad (7.141)$$

where μ is a Lagrange multiplier. We use the Euler-Lagrange equation on the integrand J of Eq. (7.141):

$$\frac{d}{d\gamma} \left(\frac{\partial J}{\partial k'_\beta} \right) - \frac{\partial J}{\partial k_\beta} = 0, \quad (7.142)$$

where k'_β is the derivative of k_β with respect to γ . This condition reduces simply to

$$\frac{\partial J}{\partial k_\beta} = 0 = 1 - \frac{\mu GQ}{2\gamma_b k_\beta^2}, \quad (7.143)$$

with the solution

$$k_\beta = \sqrt{\frac{\mu GQ}{2\gamma_b}}. \quad (7.144)$$

By examining the expressions we have derived for the betatron wavenumber of various types of focusing systems, the result in Eq. (7.144) tells us that the optimum way

to grade the strength of the focusing system is to have the solenoidal field strength be proportional to $\sqrt{\gamma}$.

We can now determine μ by substitution into the constraint equation (7.139) as

$$\sqrt{\mu} = \frac{\sqrt{2GQ}}{\lambda \text{Re}(\Lambda)} (\sqrt{\gamma_\infty} - \sqrt{\gamma_0}). \quad (7.145)$$

So, we can now find the values of k_β and ϕ_β as

$$k_\beta = \frac{\sqrt{2GQ}}{\lambda \text{Re}(\Lambda)} \frac{(\sqrt{\gamma_\infty} - \sqrt{\gamma_0})}{\sqrt{\gamma_b}}. \quad (7.146)$$

$$\phi_\beta = \frac{2GQ}{\lambda^2 \text{Re}(\Lambda)} (\sqrt{\gamma_\infty} - \sqrt{\gamma_0})^2. \quad (7.147)$$

From Eqs. (6.3), (7.101) and (7.104), it is clear that increasing the pipe radius b will have high leverage in lowering the phase advance and number of BBU e -folds in an accelerator. In fact, a figure of merit may be defined for an accelerator transport system that is just

$$\phi_\beta \text{Re}(\Lambda) = \frac{2GQ}{\lambda^2} (\sqrt{\gamma_\infty} - \sqrt{\gamma_0})^2. \quad (7.148)$$

For a given choice of energy and beam current, this figure can be minimized by using a larger pipe and higher accelerating gradient.

The DARHT-I accelerator at LANL was the first induction machine to be designed using some of these considerations [33]. Cost and availability of ferrite led to the choice of pipe radius as 7.5 cm. A Γ of 3 was chosen as a design goal for a beam current of 3 kA. The fact that the two pulsed power drive rods were close to the accelerating gap locations led to a splitting of the BBU mode impedances in the horizontal and vertical direction. This splitting led to an effective impedance that was lower than that in either plane since the mode frequencies in the two directions were different by about 20%.

In order to achieve a high beam brightness from the velvet cathode, an injector voltage of 4 MV was chosen. The machine consists of 64 cells with an accelerating voltage of 250 kV each. A minimum accelerating gap was chosen as 1.5 cm to be consistent with the breakdown strength of the vacuum electrodes while minimizing the transverse impedance. An initial magnetic field was chosen at 250 Gauss in order to avoid problems with the image displacement effect and to minimize the phase advance for corkscrew. Increasing the magnetic field with energy by a modest factor leads to a BBU exponential gain of approximately 3.

7.8 Nonlinear Focusing to Suppress BBU

7.8.1 Motivation for Nonlinear Focusing Systems

Electron beams propagating in accelerators always deviate from the axis due to misalignments of focusing elements, injection errors or “error” fields. In addition, there are a variety of instabilities that may lead to amplification of this transverse motion. It has long been known that nonlinear focusing systems will lead to *phase mix damping* of particle motion. Phase mixing occurs when particles in a thin axial slice of the beam have a distribution of betatron wavelengths. This leads to a damping of the motion of the centroid since after several oscillations the particle orbits will lose phase coherence. If the spread in betatron wavelengths is sufficiently large, some instabilities, like BBU can actually be suppressed while the behavior of others is qualitatively changed. Unless there is an instantaneous energy spread in a slice, phase mixing does not occur in linear focusing channels since the betatron frequency in a quadratic potential (which yields a linear restoring force) is independent of the amplitude of the motion. In a nonlinear channel, the potential is anharmonic so that the betatron frequency is amplitude dependent and phase mixing will occur. The focusing systems to be discussed in this section were motivated by the desire to incorporate phase mix damping.

7.8.2 Laser Generated Ion Channel

If the accelerator could be filled with a suitable low-pressure gas, a plasma channel could be produced by propagating a laser beam along the axis. When a relativistic electron beam encounters the plasma, its radial electric field expels the plasma electrons, leaving behind a positively charged ion channel, as illustrated in Fig. 7.24.

All that is required for phase mixing is that the ion density profile be non-uniform in radius. The potential well created by the ions will then be anharmonic. We will see in Sect. 7.8.3 that only a small degree of nonlinearity may be required in order to suppress instabilities. Only 0.1 mTorr pressure of a gas such as benzene or

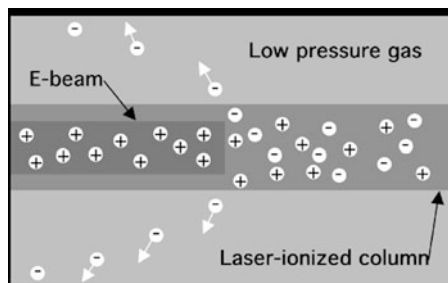


Fig. 7.24 Laser guiding scheme. The accelerator tube is filled with a dilute gas that is ionized by a laser pulse, producing a plasma column. The radial electric field of the electron beam expels the plasma electrons leaving behind a positively charged column that focuses the beam

n-diethyl aniline is required to produce a strong channel. KrF lasers producing several hundred millijoule pulses have been used to ionize channels on the order of 100 m in length [34, 35]. Today, high intensity, short-pulse lasers can ionize virtually any gas in any ionization state.

Consider a uniform density ion channel of radius a with total linear charge density λ . The radial electric field of this channel is then

$$E_r = \frac{\lambda r}{2\pi\epsilon_0 a^2} \quad \text{for } r \leq a, \quad (7.149)$$

$$E_r = \frac{\lambda}{2\pi\epsilon_0 r} \quad \text{for } r > a, \quad (7.150)$$

We can consider two extreme cases. If the beam fits within the channel, it experiences a linear focusing force and we may write its envelope equation as

$$R'' = \frac{E^2}{R^3} - \frac{2c\lambda R}{\gamma_b \beta^2 I_0 a^2}, \quad (7.151)$$

with equilibrium radius

$$R = \left[\frac{\gamma \beta^2 I_0 a^2 E^2}{2c\lambda} \right]^{\frac{1}{4}}, \quad (7.152)$$

and

$$k_\beta = \frac{1}{a} \left[\frac{2c\lambda}{\gamma \beta^2 I_0} \right]^{\frac{1}{2}}. \quad (7.153)$$

If the beam is very much larger than the channel, then we have wire-like focusing and the envelope equation becomes

$$R'' = \frac{E^2}{R^3} - \frac{2c\lambda}{\gamma_b \beta^2 I_0 R}, \quad (7.154)$$

with equilibrium radius

$$R = \left[\frac{\gamma \beta^2 I_0 E^2}{2c\lambda} \right]^{\frac{1}{2}}, \quad (7.155)$$

and an approximate k_β given by

$$k_\beta \approx \frac{2c\lambda}{\gamma_b \beta^2 I_0 E} = \frac{2c\lambda}{\beta I_0 E_n}. \quad (7.156)$$

Note the slow dependence of k_β on γ . In the case of a large or *harmonic channel* k_β varies as $\gamma^{-1/2}$ as shown in Eq. (7.153) while for a wire-like channel (or a wire) it has virtually no energy dependence as shown in Eq. (7.156).

Laser guiding has been remarkably successful in suppressing the beam breakup instability and other sources of transverse beam motion, but it is not without difficulties. Most of the troubles can be traced to the fact that the ions are not stationary on the time scale of the beam pulse. From the point of view of an ion in the channel, it experiences the radial electric field of the beam that will cause it to oscillate about the beam axis with “sloshing” frequency

$$\omega_s = \sqrt{\frac{eI}{2\pi\epsilon_0\beta cMa_b^2}}, \quad (7.157)$$

where a_b is the beam edge radius and M is the ion mass. For 10 kA and singly ionized benzene, the sloshing time can be on the order of tens of ns. The mobility of the ions can give rise to a potent instability known as ion-hose, which must be considered for long-pulse machines such as DARHT-II.

7.8.3 Phase Mix Damping of BBU

Beam breakup can grow very quickly in a high current accelerator, but the characteristic e -folding length is generally long compared to a betatron wavelength. In fact, this is implied by the condition for strong focusing

$$k_\beta^2 \gg \frac{GQ}{\gamma_b} \rightarrow k_\beta z \gg \frac{GQz}{\gamma_b k_\beta} \sim GQ\Gamma. \quad (7.158)$$

This raises the possibility that a small spread in the betatron wavenumber due to some nonlinearity in the focusing system may lead to a damping rate that is at least as large as the growth rate. If that condition can be achieved, we may expect the instability to be suppressed. We anticipate that a spread in betatron wavenumber will yield a damping rate of roughly Δk_β so that in order to suppress BBU we must have

$$\Delta k_\beta \geq \frac{GQ}{\gamma_b k_\beta}. \quad (7.159)$$

We will see that this argument works very well.

Consider the free oscillations of a system of undamped, non-interacting oscillators with a distribution of frequencies that are all labeled by their frequency k :

$$x_k'' + k^2 x_k = 0. \quad (7.160)$$

The distribution of frequencies $f(k)$ is normalized such that

$$\int_{-\infty}^{\infty} f(k) dk = 1. \quad (7.161)$$

The ensemble average of the displacement is given by

$$\bar{x}(z) = \int_{-\infty}^{\infty} f(k)x_k(z)dk. \tag{7.162}$$

Suppose all oscillators have an initial displacement of x_0 with zero initial x' . Then, the solution to Eq. (7.160) is just

$$x_k(z) = x_0 \cos(kz). \tag{7.163}$$

Let us choose $f(k)$ to be a Lorentzian as shown in Fig. 7.25,

$$f(k) = \frac{\Delta k/\pi}{(k - k_0)^2 + (\Delta k)^2}, \tag{7.164}$$

where Δk is the half width of the distribution at half height. Now we can compute \bar{x} as

$$\bar{x}(z) = \frac{x_0 \Delta k}{\pi} \int_{-\infty}^{\infty} \frac{\cos(kz)}{(k - k_0)^2 + (\Delta k)^2} dk = x_0 \cos(k_0 z) e^{-\Delta k z}. \tag{7.165}$$

We could have achieved the same result from an equation for \bar{x} that reads

$$\bar{x}'' + 2\Delta k \bar{x}' + (k_0^2 + \Delta k^2)\bar{x} = 0. \tag{7.166}$$

That is, the ensemble average oscillates with frequency $\sqrt{k_0^2 + \Delta k^2}$ and has an effective linear damping term $2\Delta k \bar{x}'$. If we had made a different choice for $f(k)$, we would not have obtained an exponential damping term. We might have obtained z^{-1} or z^{-2} for $kz \gg 1$ or some other dependence, but the result would have been a damped oscillation.

This result suggests a crude way of modeling phase mix damping of BBU. We can simply add a linear damping term to the equation of motion for the beam centroid and work through the growth theory again.

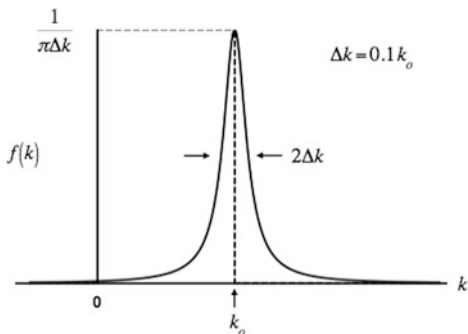


Fig. 7.25 Lorentzian distribution

We consider the case of an ion channel guided beam with the channel radius assumed to be larger than that of the beam. This is the usual condition for a long transport region, where the Rayleigh range of the laser would prevent holding a very tight focus over an extended distance. The focusing of the channel is described by Eq. (7.153), which we use to modify Eq. (7.95) to get

$$\frac{\partial^2 \xi}{\partial z^2} + \frac{1}{\gamma_b} \frac{\partial \gamma_b}{\partial z} \frac{\partial \xi}{\partial z} + \frac{2\Delta k_0}{\sqrt{\gamma_b}} \frac{\partial \xi}{\partial z} + \frac{k_0^2}{\gamma_b} \xi = \Delta, \quad (7.167)$$

where we have added a damping term characterized by the wavenumber spread $\Delta k_0/\sqrt{\gamma_b}$. Now the variable ξ stands for either x or y since there is no coupling between motion in the two planes as there was with solenoidal guiding.

If we again Laplace transform Eq. (7.167) and use (7.94) and (7.101) with $s = i\omega$, we may eliminate Δ to obtain

$$\frac{\partial^2 \tilde{\xi}}{\partial z^2} + \frac{1}{\gamma_b} \frac{\partial \gamma_b}{\partial z} \frac{\partial \tilde{\xi}}{\partial z} + \frac{2\Delta k_0}{\sqrt{\gamma_b}} \frac{\partial \tilde{\xi}}{\partial z} + \left(\frac{k_0^2}{\gamma_b} - \frac{h(s)}{\gamma_b} \right) \tilde{\xi} = 0. \quad (7.168)$$

We now make the transformation

$$\tilde{\xi} = \frac{\tilde{\Omega}}{\sqrt{\gamma_b}} e^{-\Delta k_0 \int_0^z \frac{dz'}{\sqrt{\gamma_b}}}, \quad (7.169)$$

and obtain the equation for $\tilde{\Omega}$ as

$$\frac{\partial^2 \tilde{\Omega}}{\partial z^2} + \left(\frac{k_0^2 - h(s)}{\gamma_b} \right) \tilde{\Omega} \cong 0, \quad (7.170)$$

where we have made the additional assumption that $(\Delta k_0)^2 \ll k_0^2$. Equation (7.170) is of the form (7.108) with the replacement of $k_c^2/4$ by k_0^2/γ . We could write down the solution directly, but at this point we are interested in finding the condition to suppress BBU.

Let us evaluate the exponent for the long-pulse case, where we are at the point in the pulse of maximum growth. The real part of the exponent in the expression for ξ contains the term $GQ\Gamma$ as well as a part from the transformation (7.169). Thus the total real exponent is

$$\text{Re}(\text{exp}) = -\Delta k_0 \int_0^z \frac{dz'}{\sqrt{\gamma_b}} + GQ \int_0^z \frac{dz'}{2k_0\sqrt{\gamma_b}}. \quad (7.171)$$

Both integrals have the same z dependence so that we will have no growth if

$$\Delta k_0 \geq \frac{GQ}{2k_0}. \quad (7.172)$$

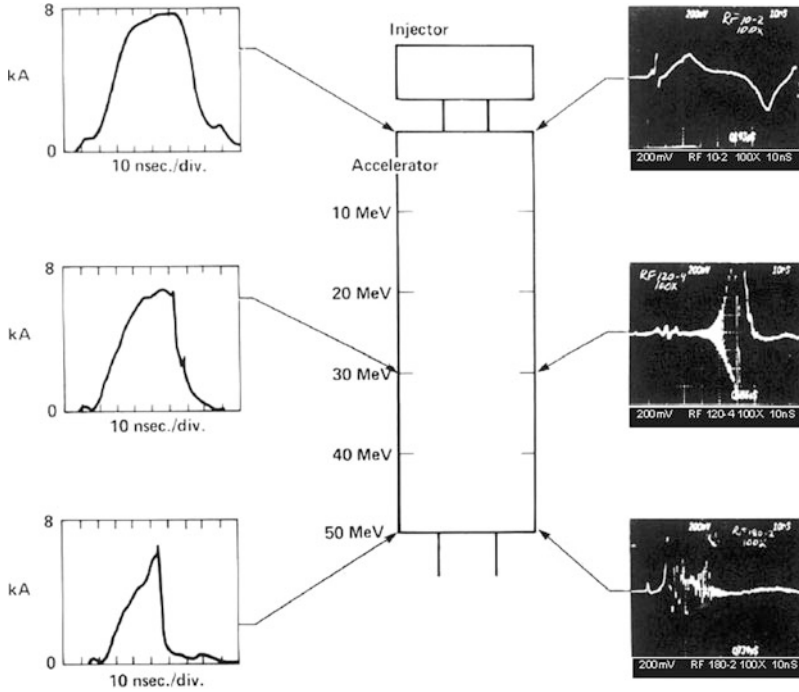


Fig. 7.26 A schematic of the ATA is shown in the *center above*. Beam current traces at different axial locations are shown on the *left*. Along the *right* side are shown outputs from loops that respond to the time changing azimuthal magnetic field caused by the rapid centroid motion of the BBU. The 830 MHz oscillations are evident in the traces

If we divide both sides of this expression by $\sqrt{\gamma}$, we will see that it is just equal to our original guess, Eq. (7.159). This result is borne out by the results of a more rigorous calculation [36].

This method of phase mix damping was used to suppress BBU in the ATA machine [34]. With the nominal 3 kGauss guide field in the accelerator, there were more than 10 e -folds of BBU growth for a 10 kA beam. By introducing low pressure benzene gas and a laser beam along the axis through a hole in the cathode, BBU was completely suppressed. Figure 7.26 shows the shortening of the beam pulse due to loss of the tail to large amplitude BBU.

The use of the laser guiding technique completely suppressed the instability and permitted transport of the full 10 kA beam without the use of any guiding magnetic field in the accelerator whatsoever. The results of this technique are shown in Fig. 7.27.

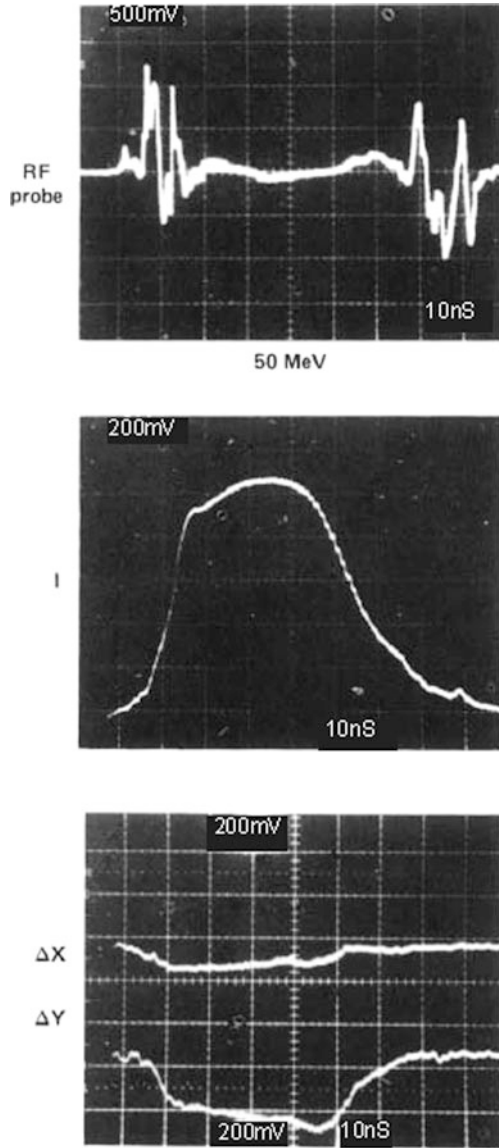


Fig. 7.27 Results of laser guiding. The *top trace* is measured at the downstream end of the accelerator (50 MeV). The body of the pulse shows an absence of 830 MHz oscillations. The *lower trace* shows the beam current at the end of the accelerator at the full 10 kA value. The beam current was fully preserved throughout the entire machine

References

1. T. Kauppila, R. Carlson, D. Moir, and R. Ridlon. Time Resolved Emittance Measurements of an Excimer-Laser-Driven Metal Photocathode. In *Proceedings of the 1991 Particle Accelerator Conference*, page 2107, San Francisco, CA, 6–9 May 1991.
2. R. Miller. Mechanism of Explosive Electron Emission for Dielectric Fiber (Velvet) Cathodes. *J. Appl. Phys.*, 84:3880, 1998.
3. D. Shiffler, M. Ruebush, M. Haworth, R. Umstatted, M. LaCour, K. Golby, D. Zagar, and T. Knowles. Carbon Velvet Field-Emission Cathode. *Rev. Sci. Instr.*, 73:4358, 2002.
4. I. Langmuir. The Effect of Space-Charge and Initial Velocities on the Potential Distribution and Thermionic Plane Electrodes. *Phys. Rev.*, 21:419, 1923.
5. H. R. Jory and A. W. Trivelpice. Exact Relativistic Solution for the One-Dimensional Diode. *J. Appl. Phys.*, 40:2294, 1969.
6. H. Ivey. Space Charge and Transient Time Considerations in Planar Diodes for Relativistic Velocities. *J. Appl. Phys.*, 23:208, 1952.
7. Y.-J. Chen, J. Boyd, and W. Turner. Degradation of Beam Brightness by Field Emission from a Cathode Shroud. Technical Report URL-98043, Lawrence Livermore National Laboratory, 1988.
8. J. Kraus. *Electromagnetics*, 3rd edition, McGraw-Hill Book Company, New York, NY, 1983.
9. E. Lee and R. Cooper. General Envelope Equation for Cylindrically Symmetric Charged-Particle Beams. *Part. Accel.*, 7:83, 1976.
10. A. Honda. On the Maximum Current for a Self-Focusing Electron Beam. *Phys. Plasmas*, 7:1607, 2000.
11. I. Kapchinskij and V. Vladimirkij. Limitations of Proton Beam Current in a Strong Focusing Linear Accelerator Associated with the Beam Space Charge. In *Proceedings of the International Conference on High Energy Accelerators and Instrumentation*, page 274. CERN Scientific Information Service, Geneva, 1959.
12. Y.-J. Chen. Corkscrew Modes in Linear Accelerators. *Nucl. Inst. Meth. A*, 292:455, 1990.
13. Y.-J. Chen. Control of Transverse Motion Caused by Chromatic Aberration and Misalignments in Linear Accelerators. *Nucl. Inst. Meth. A*, 398:139, 1997.
14. W. Nexsen, S. Allen, F. Chambers, R. Jong, A. Paul, S. Sampayan, and W. Turner. Reduction of Energy Sweep of the ETA-II Beam. In *Proceedings of the 1991 Particle Accelerator Conference*, page 3103, San Francisco, CA, 6–9 May 1991.
15. W. Nexsen, D. Atkinson, D. Barrett, Y.-J. Chen, J. Clark, L. Griffith, H. Kirbie, M. Newton, A. Paul, S. Sampayan, A. Throop, and W. Turner. The ETA-II Induction Linac as a High Average Power FEL Driver. In *Proceedings of the 11th International FEL Conference*, page 54, Naples, FL, 28 Aug.–1 Sept. 1989.
16. W. Turner, S. Allen, H. Brand, G. Caporaso, F. Chambers, Y.-J. Chen, F. Coffield, F. Deadrick, T. Decker, L. Griffith, D. Lager, W. Mauer, W. Nexsen, A. Paul, V. Renbarger, and S. Sampayan. Reduction of Beam corkscrew Motion on the ETA-II Linear Induction Accelerator. In *Proceedings of the 1990 Linear Accelerator Conference*, page 435, Albuquerque, NM, 10–14 Sept. 1990.
17. S. Allen, H. Brand, F. Chambers, Y.-J. Chen, F. Coffield, F. Deadrick, L. Griffith, D. Lager, W. Mauer, W. Nexsen, A. Paul, S. Sampayan, and W. Turner. Measurements of Reduced Corkscrew Motion on the ETA-II Linear Induction Accelerator. In *Proceedings of the 1991 Particle Accelerator Conference*, page 3094, San Francisco, CA, 6–9 May 1991.
18. Y.-J. Chen. Beam Control in the ETA-II Linear Induction Accelerator. In *Proceedings of the 1992 Linear Accelerator Conference*, page 540, Ottawa, Canada, 24–28 Aug. 1992.
19. S. Allen and E. Scharlemann. The ETA-II Linear Induction Accelerator and IMP Wiggler: A High-Average-Power Millimeter-Wave Free-Electron-Laser for Plasma Heating. In *Proceedings of the 9th International Conference on High Power Particle Beams*, page 247, Washington, DC, 25–29 May 1992.
20. S. Allen, private communication.

21. D. Lager, H. Brand, W. Mauer, F. Coffield, F. Chambers, and W. Turner. Artificial Intelligence Techniques for Tuning Linear Induction Accelerators. In *Proceedings of the 1991 Particle Accelerator Conference*, page 3085, San Francisco, CA, 6–9 May 1991.
22. B. Kulke, T. Innes, R. Kihara, and R. Scarpetti. Initial Performance Parameters on FXR. In *Proceedings of the 15th IEEE Power Modulator Symposium*, page 307, Baltimore, MD, 14 June 1982.
23. R. Scarpetti and J.-M. Zentler, private communication.
24. V. Neil. The Image Displacement Effect in Linear Induction Accelerators. Technical Report UCID-17976, University of California, 1978.
25. R. Adler, B. Godfrey, M. Campbell, D. Sullivan, and T. Genoni. The Image-Displacement Effect in Intense Electron Beams. *Part. Accel.*, 13:25, 1982.
26. R. B. Miller, B. M. Marder, P. O. Coleman, and R. E. Clark. The Effect of Accelerating Gap Geometry on the Beam Breakup Instability in Linear Induction Accelerators. *J. Appl. Phys.*, 63:997, 1988.
27. R. Helm, G. Loew, and W. Panofsky. Beam Dynamics. In R. B. Neal, editor, *The Stanford Two-Mile Accelerator*, page 168, W. A. Benjamin, Inc., New York, NY, 1968.
28. V. Neil and R. Cooper. Coherent Instabilities in High Current Linear Induction Accelerators. *Part. Accel.*, 1:111, 1970.
29. R. Briggs. Suppression of Transverse Beam Breakup Modes in an Induction Accelerator by Gas Focusing. Technical Report UCID-18633, University of California, 1980.
30. E. Lifshitz and L. Pitaevskii. *Physical Kinetics*, Pergamon Press, New York, NY, 1981.
31. C. Ekdahl, E. Abeyta, P. Aragon, R. Archuleta, R. Bartsch, H. Bender, R. Briggs, W. Broste, C. Carlson, K. Chan, D. Dalmas, S. Eversole, D. Frayer, R. Gallegos, J. Harrison, T. Hughes, E. Jacquez, D. Johnson, J. Johnson, B. McCuistian, N. Montoya, C. Mostrom, S. Nath, D. Oro, L. Rowton, M. Sanchez, R. Scarpetti, M. Schauer, M. Schulze, Y. Tang, A. Tipton, and C. Tom. Long-Pulse Beam Stability Experiments on the DARHT-II Linear Induction Accelerator. *IEEE Trans. Plasma Sci.*, 34:460, 2006.
32. G. Caporaso and A. Cole. Design of Long Induction Linacs. In *Proceedings of the 1990 Linear Accelerator Conference*, page 281, Albuquerque, NM, 10–14 Sept. 1990.
33. P. Allison, M. Burns, G. Caporaso, and A. Cole. Beam-Breakup Calculations for the DARHT Accelerator. In *Proceedings of the 1991 Particle Accelerator Conference, San Francisco*, page 520, San Francisco, CA, 6–9 May 1991.
34. W. Martin, G. Caporaso, W. Fawley, D. Prosnitz, and A. Cole. Electron-Beam Guiding and Phase-Mix Damping by a Laser-Ionized Channel. *Phys. Rev. Lett.*, 54:685, 1985.
35. G. Caporaso, F. Rainer, W. Martin, D. Prono, and A. Cole. Laser Guiding of Electron Beams in the Advanced Test Acceleration. *Phys. Rev. Lett.*, 57:1591, 1986.
36. G. Caporaso and A. Cole. High Current Electron Transport. In M. Month and M. Dine, editors, *The Physics of Particle Accelerators*, page 1615, Brookhaven National Laboratory, Upton, NY, 1992. AIP Conference Proceedings 249.